Analyzing the oxidation of in situ cleaved Transition Metal Dichalcogenides

Aarts, Resi

Analyzing the oxidation of *in situ* cleaved Transition Metal Dichalcogenides
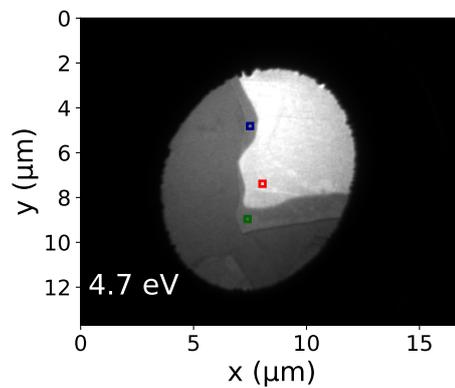
THESIS

submitted in partial fulfillment of the
requirements for the degree of

MASTER OF SCIENCE

in

PHYSICS

Author :	Resi Aarts
Student ID :	s2196492
Supervisor :	Prof.dr.ir. Sense Jan van der Molen
Second corrector :	Prof.dr.ir. Tjerk Oosterkamp

Leiden, The Netherlands, August 29, 2023

Analyzing the oxidation of *in situ* cleaved Transition Metal Dichalcogenides

Resi Aarts

Huygens-Kamerlingh Onnes Laboratory, Leiden University
P.O. Box 9500, 2300 RA Leiden, The Netherlands

August 29, 2023

Abstract

In this research, we study the oxidation process of the Transition Metal Dichalcogenide (TMD) niobium diselenide, $NbSe_2$. TMDs are a category of van der Waals materials, of which samples are obtained by exfoliation. The measurements are performed with the Low Energy Electron Microscope (LEEM), which measures reflectivity at different energy, resulting in the so-called IV curves. To analyze oxidation, we have developed a new method to obtain *in situ* exfoliated flakes in the LEEM set-up. First, we measure *in situ* cleaved $NbSe_2$ flakes (bulk). The reflectivity upon adding (pure) oxygen is followed. Additionally, the reflectivity of *ex situ* cleaved $NbSe_2$ flakes is assessed. Here, an intensity boundary between flake's edge and center is recognized. The reflectivity measurements show that the electronic structure is different across the boundary: a V-shaped reflectivity minimum appears, which sharpens over time upon oxidation. The boundary is further researched with Atomic Force Microscopy and Energy Dispersive X-ray analysis. Additionally, we perform roughness analysis and Principal Component Analysis. The latter provides an alternative method to follow the change in electronic properties over time. We propose that already degraded $NbSe_2$ flakes are more susceptible to oxidatin damage, compared to *in situ* exfoliated flakes. Upon further measurements, the *in situ* cleaved samples do not show any degradation signs, therefore we attribute the presence of an intensity contrast with the associated IV features, to oxidized $NbSe_2$.

Contents

Chapter 1

Introduction

The dimensionality of a material influences properties of materials. The world as we view it is three-dimensional, and all materials in it as well, as one would assume. This, however, changes with the definition of properties on quantum scale. Specifically, dimensionality is determined by number of degrees of freedom of electrons. For example, electrons in 3D materials have three degrees of freedom (spin aside) and can move freely in a 3D space. We can also define lower dimensional materials: in 2D materials, the electrons are confined to planar motion, and are restricted in the third direction. From this confinement, interesting physics arises, such as the Quantum Hall Effect [1]. By applying a magnetic field in the third direction, the electron energy levels become quantized and the prevriously constant Density Of States (DOS), changes to a Dirac comb.

An intensively studied 2D material is graphene, which was first isolated from bulk graphite by Novoselov et al. in 2004 [2]. Graphene was a promising system to observe the exotic Quantum Hall Effect [3, 4] as well as high electron mobility [5]. It incited the research into similar materials: the so-called van der Waals (vdW) materials. These layered materials are characterized by weak out-of-plane interaction (vdW forces) and strong in-plane covalent bonds. Due to these weak out-of-plane bonds, the layers can be separated easily: exfoliation can be practiced with a household staple: scotch tape [6]. Among vdW materials, electronic properties differ. Graphene, for instance, behaves as a semi metal, whereas hexagonal Boron Nitride (hBN) is an insulator. A subcategory is formed by Transition Metal Dichalcogenides (TMDs), which are suitable for fabrication of electronic devices. Interestingly, the number of layers is a de-

7

cisive factor in the electronic behaviour. Specifically, while bulk TMD exhibit an indirect bandgap [7], TMDs monolayers have a direct bandgap of around 2 eV which lies in the visible light range [8]. Therefore, it can be exploited in (opto)electronic devices like transistors or photodetectors [9, 10]. Another application of TMDs is found in valleytronics [11]; electrons distribute unequally over valleys in reciprocal space and this polarization can be tuned for systems with broken inversion symmetry. The broken inversion symmetry in TMDs occurs because inversion center is located in between layers, such that the inversion switches at successive layers. Lastly, by stacking different TMD monolayers, one can design materials with desired quantum properties.

The applications that TMDs have for fabrication of nanodevices are promising. However, as the field of study arose only a decade ago, there are still uncharted details and features of these TMDs. Also, electronic devices like Field Effect Transistors (FETs) make use of monolayer TMD, of which performance can deteriorate due to oxidation [12]. Therefore, we need to understand the effect of oxidation on the band structure of TMDs.

In this research the band structure of molybdenum disulfide, MoS_2 and niobium diselenide, $NbSe_2$, is studied. Furthermore, the effect of oxidation the band structure is investigated. We first treat the theoretical background for TMDs, delving into their properties, band structure and spectroscopic techniques to characterize TMDs. Low Energy Electron Microscopy (LEEM) is employed to investigate the characteristics of TMDs. Atomic Force Microscopy (AFM) and Scanning Electron Microscopy (SEM) are used for further interpretation of the LEEM results. Chapter 3 explains the application of these methods and a novel exfoliation method. Subsequently, the obtained results and discussion are described in chapter 4. Finally, we draw conclusions about the results in chapter 5 and discuss the implications and further research.

Chapter 2

Theoretical background

Tthe vdW materials Transition Metal Dichalcogenides (TMDs) have been introduced, of which the structure and properties are now described in more detail. Also, we will discuss what the band structure is and how this determines electronic properties. We show how the band structure is mapped with LEEM, with a technique called Angle Resolved Reflectivity Electron Spectroscopy (ARRES). Lastly, the sample degradation due to oxidation in TMDs is studied.

2.1   Band structure of Transition Metal Dichalcogenides

In TMDs, a transition metal atom (e.g. molybdenum, tungsten, niobium) is sandwiched between two chalcogens (sulfur, selenide, tellurium), as is shown in figure 2.1. One monolayer TMD thus consists of three atomic layers. The thickness of such a monolayer is approximately 0.7 nm [9]. Figure 2.1 displays
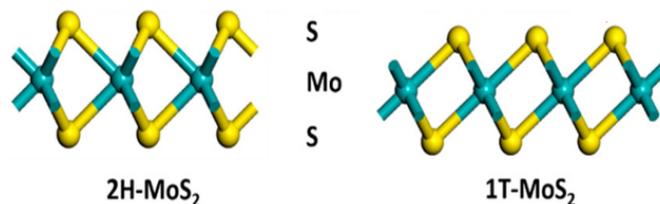

Figure 2.1: *A schematic three-dimensional view of a TMD. The transition metal is Molybdenum (Mo) with Sulfur (S) atoms as chalcogens. MoS$_2$ occurs in two polytypes: 2H and 1T. Modified from [13].*

two polytypes with a different arrangement of chalcogen atoms: the octohedral
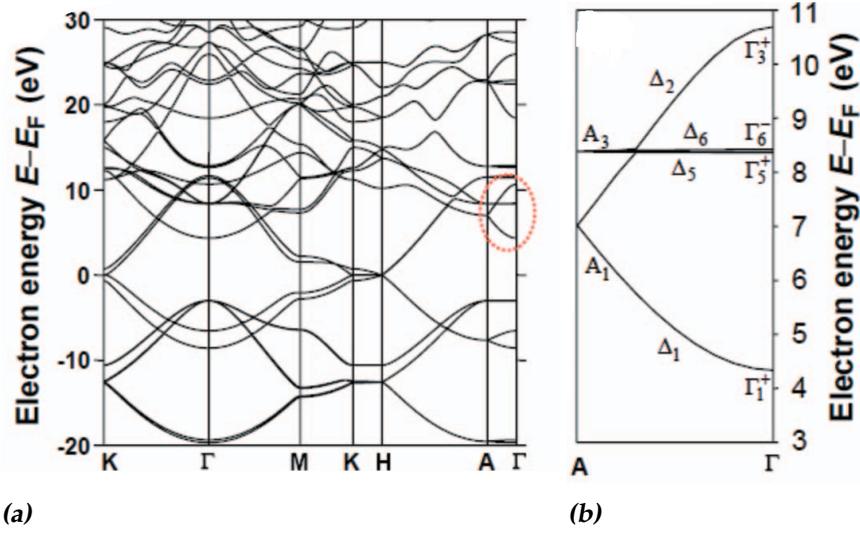
Figure 2.2: **(a)**: *The theoretical band structure of graphite. A red dotted circle can be seen around a conduction band that splits into two in region* **A** *to* Γ*.* **(b)**: *Zoom in on conduction band, known as the interlayer state. Modified from [15].*

1T phase and hexagonal 2H phase. As the 1T phase is metastable, we work with with 2H- MoS_2 [13]. Furthermore, niobium diselenide, $NbSe_2$, will be studied, of which also the 2H polytype is the most stable [14]. The hexagonal structure of the TMDs leads to the band structure, which determines electronic properties. Therefore, we now discuss the nature of this lattice.

The band structure is a representation of allowed electron energies. Allowed energies form the energy bands while energy gaps are forbidden energies. An example of a band structure is depicted in figure 2.2a. The bands up to the Fermi energy, which is located at $E - E_F = 0$ in figure 2.2a, are filled with electrons. The bands above and below the Fermi level are called the conduction and valence bands respectively. The difference between these bands defines the band gap. The location of E_F with respect to these bands is decisive for electronic properties; in insulators and semiconductors E_F lies between them, like in figure 2.2a. For metals, the bands interesect at E_F which implies that valence electrons can move freely. Figure 2.2a shows that the band structure is a function of energy E versus momentum vector **k**. Namely, the reciprocal lattice is defined in **k**-space and the **k**-vector determines its periodicity. The repetitive unit in this lattice is called a Brillouin Zone (BZ), which is constructed through the diffraction pattern. Vector **k** consists of a parallel (i.e. in-plane) and perpendicular component: $k_{||}$ and $k_{\perp}$. Figure 2.2a shows both: from **K** to Γ and **A** to Γ respectively. The $k_{||}$ component makes up the BZ, of which an example can be seen in figure 2.3.
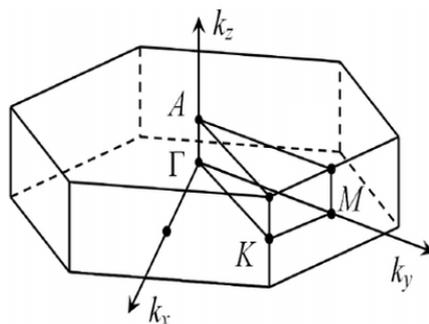
Figure 2.3: *Three-dimensional sketch of the first hexagonal Brillouin Zone of a hexagonal lattice. Black dots mark the high-symmetry points. In-plane lie: Γ, M, K and K'. Out-of-plane:* **A**. *Modified from [16].*

Figure 2.3a shows the high-symmetry points: the Γ-point lies central, **K**- and **K'**- points on the corners of the hexagonal BZ and the **M**-point is situated on the center of edges.

The conduction band in the Γ- **A** region is circled and zoomed in on, see figure 2.2b. This band is continuous for graphite, but splits in layered graphene. As the band is located between atomic layers, it is known as the interlayer state. The interlayer state is absent in the monolayer and can be understood with a Fabry-Pérot resonator model [17]. Each layer is regarded as a semitransparent mirror which transmits the electron if the energy matches with the graphene's energy band and reflects it if not. Consequently, it is transmitted or reflected upon encountering the next layer. The resulting electron waves with different phases can constructively and destructively interfere and this interference is shown with the LEEM.

2.2   Low Energy Electron Microscopy

The measurements in this research are conducted with the Low Energy Electron Microscope (LEEM) at Leiden University (ESCHER design). With the LEEM, a sample is irradiated with an electron beam and the interaction between electrons and the sample form an image. Light and dark areas highlight the areas of respectively high reflectivity and absorbance of electrons. Electrons have a smaller wavelength than light and in this way, structures smaller than the diffraction limit of light can be observed. Additionally, information about crystal structure can be obtained since the electron wavelength is in the order of the atomic lattice constant (a few Å). Commonly-used electron microscopy tech-
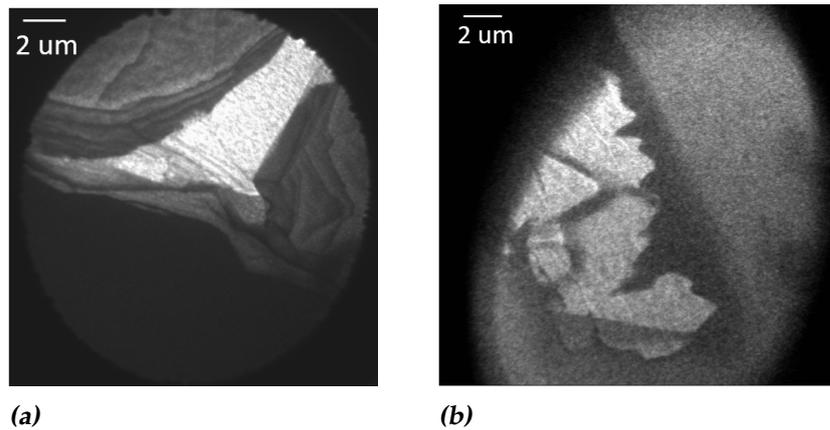
***Figure 2.4: (a)**: Bright Field (BF) LEEM image of NbSe$_2$, at energy 5.7 eV. **(b)**: Dark Field (DF) LEEM image of NbSe$_2$, at energy 25.2 eV.*

niques like Scanning Electron Microscopy (SEM) and Transmission Electron Microscopy (TEM) use electrons up to 30 kV and 300 kV respectively [18]. These high-energy electrons damage the sample and thereby limit measurement time. In contrast, the low-energy electrons (0 - 50 kV) used in LEEM, only penetrate the sample slightly. The limited penetration depth makes LEEM a surface-sensitive technique. Therefore, LEEM images give an opportunity to study interactions in the shallow surface layers of the sample.

2.2.1   Imaging with LEEM

In LEEM, different imaging techniques can be used. First, bright-field (BF) imaging is practiced by selecting only the specularly reflected electrons, also called the (0,0) beam. Advantageously, the secondary electrons i.e. the electrons that scatter inelastically from the sample surface, are excluded. These secondary electrons can blur the image. An example of a BF image is shown in figure 2.4a. Different forms of contrast can be distinguished in LEEM images: (i) phase contrast and (ii) amplitude contrast [19]. Phase contrast arises near to the edges if the image is slightly out-of-focus. Amplitude contrast is caused by a different reflectivity amplitude which can arise from different layer thicknesses. With the first order diffraction spots in the Low Energy Electron Diffraction (LEED) pattern, we can select electrons with non-normal incidence. Images which are formed from a first order diffracted beam, are called (DF). Figure 2.4b provides an example of DF imaging. With this technique, areas with the same crystal orientation are identified.

2.3 Angle-Resolved Reflectivity Electron Spectroscopy

2.3.1 LEEM and the electronic structure

With LEEM, one can measure electron reflectivity spectra, i.e., reflected intensity as a function of energy, also called IV curves. An example IV curve for bulk MoS_2 is shown in figure 2.5. The dips in reflectivity in figure 2.5 yield infor-
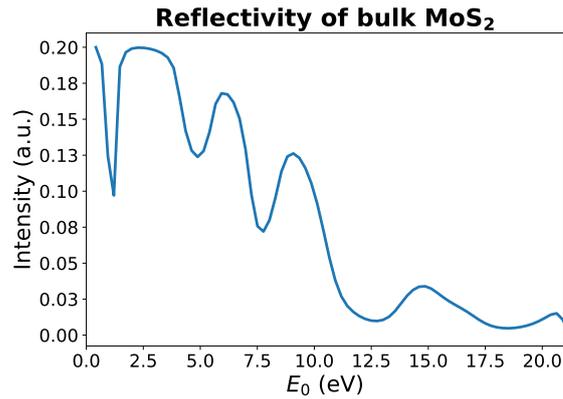
Figure 2.5: *Theoretical reflected intensity versus energy, called an IV measurement, of bulk MoS_2. The reflectivity minima reflect the presence of states. Calculated from [20].*

mation about the electronic structure. If the electron energy is resonant with an unoccupied state, it has a high probability of travelling into the material, causing a minimum in reflectivity. Figure 2.5 shows a minimum around 5 eV which represents the interlayer state discussed in section 2.1. This resonance enables us to count the number of layers in few-layer material [15]: for n layers, the interlayer state splits in $n - 1$ minima. For bulk, the $n - 1$ minima are indistinguishable and result in one minimum around 5 eV, as seen in figure 2.5.

A visualization of these states is given by solving the electron scattering problem. For MoS_2, this is performed in [17] and the result is provided in figure 2.6. The probability density for energies ranging from 0 to 10 eV is plotted against the depth (in the material) d in Å. For $d > 0$, the probability density is determined by the interference of incoming and outgoing waves. As energy increases, the wavelength decreases and the interference rings are packed more densely. Inside the material ($d \leq 0$), high probability density indicates a state. We see for all three plots in figure 2.6, a state around 1 eV, present in figure 2.8. It is centered in the first layer. Then, for the 2 layers, we observe that the interlayer state around 5 eV, which is indeed located between layers. This state splits in two in the 3-layer MoS_2.
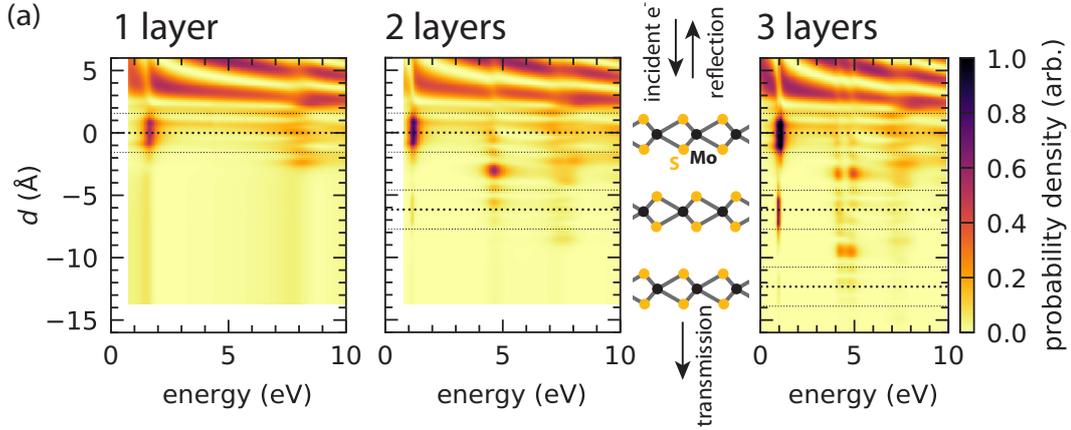
Figure 2.6: *Probability density of electron waves in few-layer MoS_2. Here, the waves enter the material at $d = 0$. At $d > 0$, we observe the interference of electron waves outside the material. For $d < 0$, high probability density indicates the presence of states. Taken from [17].*

2.3.2 Angular dependence of reflectivity in LEEM
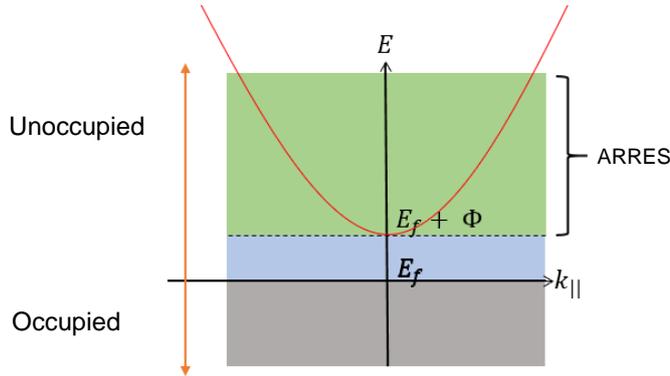
Figure 2.7: *Diagram of energy E versus $k_{||}$ which displays in which energy range the Angle Resolved Reflectivity Electron Spectroscopy (ARRES) technique operates: green area. Dashed horizontal line: zero-energy for LEEM experiments, given by $E_f + \Phi$. Above E_f, states are unoccupied, below E_f occupied. Red parabola: electron vacuum dispersion.*

Figure 2.5 depicts the energy dependent reflectivity at normal incidence which means $k_{||}$ equals zero. Then, the reflectivity at the Γ-point is mapped. For analysis of the complete band structure, the angle of incidence is varied over the first BZ. The technique, where E and $k_{||}$ are varied, is called Angle Resolved

Reflected-Electron Spectroscopy (ARRES). The ARRES technique operates at energies above the vacuum energy: $E_f + \Phi$, indicated with the green area in figure 2.7. Figure 2.7 demonstrates that ARRES maps unoccupied states. Let us now analyze an ARRES plot to find out how. Figure 2.8b shows a theoret-
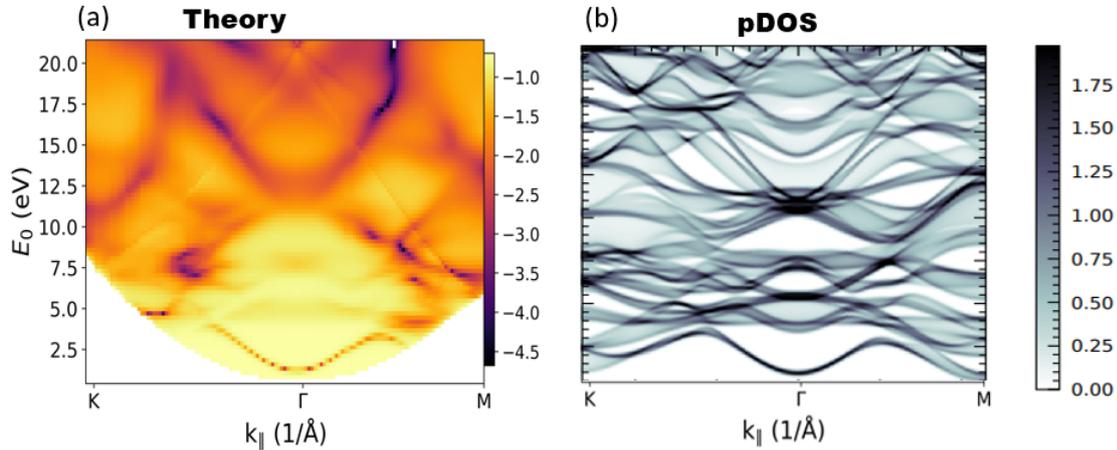
Figure 2.8: **(a)**: *Theoretical Angle Resolved Reflectivity Electron Spectroscopy (AR-RES) plot, which maps the full unoccupied band structure.* **(b)**: *projected DOS (pDOS) of MoS$_2$. A great correspondence is observed between high ARRES intensity and the presence of bands in the pDOS. Modified from [20].*

ical ARRES plot of bulk MoS$_2$ and the linecut along $k_{||}$ gives the IV curve in figure 2.5. As with an IV-curve measurement, we expect that the availability of unoccupied states in the material increases the absorption probability and thus decreases reflectivity. In the ARRES spectrum, this shows as a low reflectivity $R(E, k_{||})$. Vice versa, areas of high reflectivity indicate absence of unoccupied states. Therefore, the unoccupied band structure is mapped by ARRES. To verify the theoretical ARRES, we compare it with with the projected DOS, pDOS, (in the z-direction) in figure 2.8b. Namely, figure 2.8a illustrates that high reflectivity in ARRES plots corresponds to presence of states (i.e. black bands) in figure 2.8b and vice versa.

2.4   Oxidation

Oxidation is the reaction between oxygen and molecules which can change electronic properties. The oxidation of metal surfaces consists of multiple steps. First, the oxygen molecules adsorb on the surface on which they then diffuse. Subsequently, oxygen diffuses into the first layers of the material and in this

step, oxygen atoms interact with the TMD. This can result in a chemical reaction. Besides diffusion and molecular interactions, the oxidation depends on environmental factors like temperature and pressure. Dependent on the exact conditions, different oxidation states can arise [21].

2.4.1   Oxidation process in TMDs

The effect of oxygen varies across different materials; bulk Molybdenum Disulfide (MoS_2) is stable in the presence of oxygen, while Niobium Diselenide ($NbSe_2$) is instable and sensitive to oxygen adsorption [22]. To note though, is that few-layer MoS_2 is susceptible to oxidation. Also, Qiu et al. reported that the performance of their MoS_2 Field-Effect Transistor decreased with a factor 100 by adsorption of oxygen and water [12]. Also, Liu et al. found that monolayer MoS_2 suffers from oxidation [23]. Since the adsorbed layer formed just a thin layer, annealing reversed the effect.

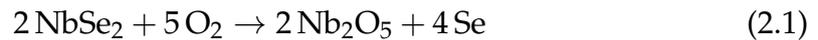To observe oxidation in the LEEM, we will use the more sensitive $NbSe_2$. The following chemical reaction takes place during the oxidation of $NbSe_2$ [24, 25]:

$$2\,NbSe_2 + 5\,O_2 \rightarrow 2\,Nb_2O_5 + 4\,Se \tag{2.1}$$

In this reaction, the Se atoms are replaced by O atoms leading to the formation of Nb_2O_5 and individual Se atoms. The strength of this bond is determined by the electronegativity of the chalcogen atoms [23]. For a smaller electronegativity, more electrons are transferred to the O atom which results in a stronger Metal - O bond. The Nb_2O_5 is amorphous i.e. has no long range crystalline structure [25, 26]. As LEEM images give information about crystal structure via the diffraction pattern, we are able to follow this structural change. Furthermore, it is expected that a layer of a few nm of Nb_2O_5 is formed at the surface, increasing the height [25, 27].

The time scale differs among experiments: in [25], the $NbSe_2$ was brought in air for 21 days at room temperature, whereas it is reported in [27], that the TMD (WSe_2) was treated with O3 (ozone) at 150 °C for 2h and at 200 °C for 1h. Some experiments were performed over longer time periods: several months [28] up to one year [29–31]. The oxygen diffuses through the material and its velocity v scales with $\sqrt{t}$ and is therefore expected to 'saturate' over time. Also, oxidation is self-limiting as the newly-formed oxide layer hinders further diffusion of oxygen the subsurface region [27].

For the flakes of TMDs, the oxygen diffuses into the flake via the edges faster
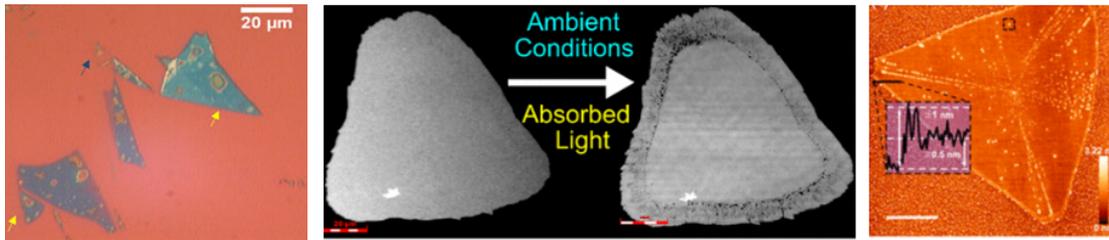
(a) *Speckles on thin flake MoS$_2$. From [29].*   **(b)** *Left: LSCM photograph of WS$_2$ flake. Right: Measured height of islands. Modified from [28].*

Figure 2.9: *Examples of flake degradation in MoS$_2$ and WS$_2$ due to oxidation, observed with different measurement techniques:* **(a):** *Optical microscope,* **(b)** *Left: Laser scanning confocal micrograph (LSCM). Right: Atomic Force Microscopy (AFM).*

than on top of the material [26, 30]. This difference can be explained via cleavage of vdW materials: an edge arises when the crystal is cleaved perpendicular to the basal plane. The covalent bonds are broken and adsorbates like oxygen are more likely to interact with these loose bonds [32]. Also, the crystal edges exhibit a higher concentration of sulfur vacancies and this higher concentration has been linked to more oxidation degradation [29]. This correlation was also observed by Kotsakidis et al. [28]. These sulfur vacancies are sample defects that occur more often for Chemical Vapor Deposition (CVD) grown layers than layers that were obtained by mechanical exfoliation [29].

2.4.2   The influence of water and light on oxidation

For oxidation, we consider that oxidation in air is different than exposure to pure oxygen. The air also contains water which plays a role in the oxidation, as described in [31]: high humidity increased the oxidation damage in monolayers WS$_2$ and MoS$_2$. This influence of water in air is also reported in [29], where speckles were observed on both thin and bulk MoS$_2$ flakes. The speckles on thin flakes are depicted in figure 2.9a and were attributed to absorbed water molecules. Budania et al. reasoned this, because the degradation was reversible upon annealing, which can be explained only by the evaporation of water molecules.

Another factor to consider is light. To test the influence of light, Myers and Montet exposed single NbSe$_2$ crystals to air and illuminated the crystals with fluorescent light [30]. Interestingly, only the flakes exposed to the light were affected: they did not show a diffraction pattern and lost their red colour. Similarly, the oxidation of WS$_2$ is photo-induced [28]. Only a combination of ambi-

ent air with light (after a period of up to ten months) would give rise to small islands on the sample. The islands can be seen in figure 2.9b. With AFM, it was determined that the islands were around 1.14 nm high [28] (with respect to the original sample surface). The islands exhibited a shift in photoluminiscence (PL), which indicates that the electronic structure changed upon oxidation. The physical process resulting in the change in the PL spectrum was not determined, which shows that damage due to oxidation requires further research.

Chapter 3

Methods

This chapter discusses the used methodology to study the oxidation in niobium diselenide $NbSe_2$. First, the LEEM set-up is explained. Additionally, a method to reduce noise of the electron gun in the set-up is treated. Then, we study the method of in situ (i.e. vacuum) exfoliation of Transition Metal Dichalcogenides (TMDs). Subsequently, section 3.3 goes into detail about methods to oxidize the $NbSe_2$ and an overview of the samples is given. To investigate the oxidation state we use several techniques: Atomic Force Microscopy (AFM) and Scanning Electron Microscopy (SEM) & Energy Dispersive X-ray (EDX). Furthermore, Principal Component Analysis (PCA) and roughness analysis are performed to obtain extra information on the electronic structure.

3.1 LEEM set-up

A schematic overview of the LEEM set-up is depicted in figure 3.1. First, a cold field emission gun (of Tungsten) emits electrons at -15 keV, with an energy spread of approximately 0.25 eV [33]. The gun potential is negative to keep the rest of the set-up on ground. We will now follow the electron trajectory through the set-up.

The angle of incidence of the electron beam on the sample can be varied with deflector 1. After, the beam is focused by a gun lens and condenser lens respectively. The electron beam goes through a magnetic prism array which deflects the electrons under a right angle towards the objective lens. An illumination aperture,displayed as the top diagonal in figure 3.1 can be placed inside the image plane of the prism to only illuminate a certain sample area with elec-
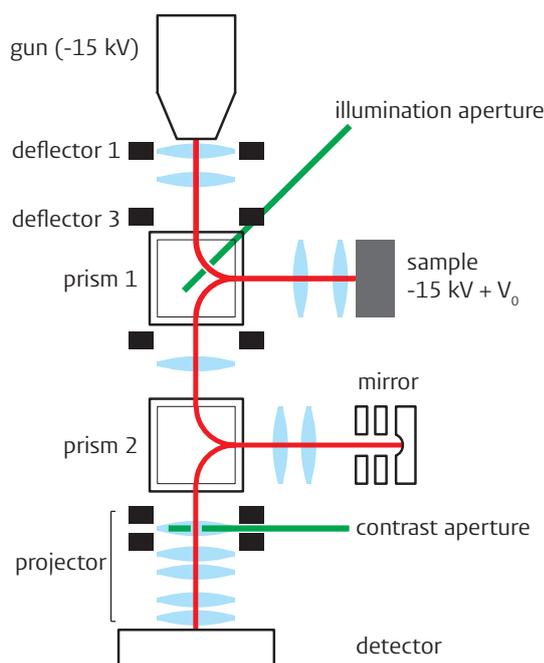
Figure 3.1: *LEEM set-up schematic. Electrons travel the red path, from the gun to the detector. Lenses can be seen in blue and apertures in green. Prism 1 deflects the beam 90 °through the sample. The electrons are partly reflected and follow their pathway back to prism 1. Prism 2 deflects under a right angle to the electrostatic mirror. Then, upon reflection, the electrons are deflected towards the detector. Obtained from [19].*

trons. Next, the electrons are decelerated by an applied potential of -15 keV + V_0. The landing energy is varied with V_0, theoretically in the range of about 0 to 100 eV [33]. For $V_0 < 0$, the electrons do not have enough energy to hit the sample, and all are reflected, which is called mirror mode. For $V_0 > 0$, the electrons interact with the sample surface and are reflected back partially. The electrons are accelerated and focused by a magnetic lens. Upon hitting the first magnetic prism again, they get deflected 90 degrees. A second prism leads the electrons to an electrostatic mirror which corrects for for spherical and chromatic aberrations caused by the cathode objective lens (up to fifth order) [33]. The electrostatic mirror improves the spatial resolution from 5 nm to < 2 nm [33]. Next, a contrast aperture selects the electrons scattered under a certain angle from the sample, for example only the (0,0) beam. Finally, electrons find their way to the CCD detector, where an imaged is formed. Furthermore, we perform Photo Emission Electron Microscopy (PEEM) with an Hg lamp. The UV light excites electrons from the sample which are recorded by the detector, resulting in a PEEM image.

3.1.1 µ-LEED

We already touched upon the illumination aperture visible in figure 3.1 and now we discuss an imaging technique associated with this aperture: very -Low Energy Electron Diffraction (LEED), also called µ-LEED. With LEED, the diffraction pattern that arises at the backfocal plane of the objective lens is imaged, which contains information about the crystal structure (see section 2.1). One speaks of µ-LEED, if the illuminated sample area is restricted with an illumination aperture. In this manner, the diffraction pattern obtain insights about the specific illuminated area. We measure with illumination apertures of around 1 µm diameter.

3.1.2 Noise reduction

The basics analysis steps consist of (i) channelplate correction and (ii) drift correction, which are described in [34]. Additionally, we correct the diffraction IV curves for noise caused by the electron gun. The gun has a fluctuating intensity which causes noise, which can be corrected for. Furthermore, we use the dispersion of the gun to do additional noise reduction. Namely, electrons leaving the gun have slightly different kinetic energy E_k (a FWHM of 0.25 eV [33]), as explained in [35]. In the LEEM set-up, the electrons are deflected 90 degrees before hitting the sample by the magnetic prism (see figure 3.1). The difference ΔE_k leads to a different orbital radius r via:

$$R = \frac{mv}{qB} \tag{3.1}$$

with m mass electron v velocity of electron, related with E_k as $E_k = \frac{1}{2}mv^2$. The q is electron charge, and B magnetic field. When electrons have a different r, they end up at a different position on the detector i.e. a different pixel in the image. This results in an elongated diffraction spot, in the dispersive direction of the prisms in figure 3.1.

We take a linecut along this direction, such that we average n frames with different intensity to reduce noise with $\sqrt{n}$. Before averaging, we translate IV curves from different pixels such that they align with the middle pixel in the linecut. For this, the energy (in eV) per pixel δ was calculated in [35]. Mathematically, the intensity I_n is corrected as follows:

$$I_{shift}(E) = \frac{1}{N} \sum_{n=1}^{n=N} I_n(E - \delta \cdot n) \tag{3.2}$$

With formula 3.2 a corrected average is computed. To improve this formula, we normalize the IV curves: the IV curves for different pixels along the linecut have a different intensity in the mirror mode (where $E < 0$). A normalization factor A_n is computed as:

$$A_n = \frac{\sum I_n(E < 0)}{\sum I_{max,pix}} \tag{3.3}$$

The corrected IV curve intensity is then calculated via:

$$I_{n,norm} = A_n(E) \cdot I_n(E) \tag{3.4}$$

The final, noise reduced IV curve is obtained with averaging the $I_{n,norm}$ over n pixels.

Noise reduction in real space LEEM images

The above described noise reduction can not be applied in real space, as the elongated diffraction spot is absent. Therefore, real space IV curves are filtered with a Wiener filter (see [36] for documentation). This filter uses cross-correlation to estimate the power spectral density of the noise. It computes filter coefficients that minimize the RMSE between the original and filtered signal.

3.2   In situ exfoliation

We exfoliate 2H-MoS$_2$ and 2H-NbSe$_2$ crystals in air with the scotch tape method [6]. The layers are peeled off since the sticking force of scotch tape is larger than the vdW forces between layers. To exfoliate in situ (i.e. in vacuum), the final exfoliation step takes place in the load lock. This load lock is used to load the sample and is connected to the sample chamber via the transfer chamber.

To perform in situ exfoliation, we use a screw of which the back is covered in Kapton tape (polyimide film, DuPont, Wilmington, USA), which is vacuum compatible. The tape is tightened with a metal wire onto the screw, and the screwhead must be free of tape. The screw is stamped onto freshly cleaved TMD crystal. We put a clean Si substrate in the sample holder. Via the Kapton tape, the screw is glued to a substrate. A schematic overview of this part of the set-up is depicted in figure 3.2a and figure 3.2b provides a photo. The sample holder, with the screwhead pointed downwards is brought into the load lock. We pump the loadlock down to 1e-7 mbar.

Then, we turn the transfer arm in the load lock such that an aluminium cup-shaped tool knocks off the screw with the Kapton tape. We have fabricated this
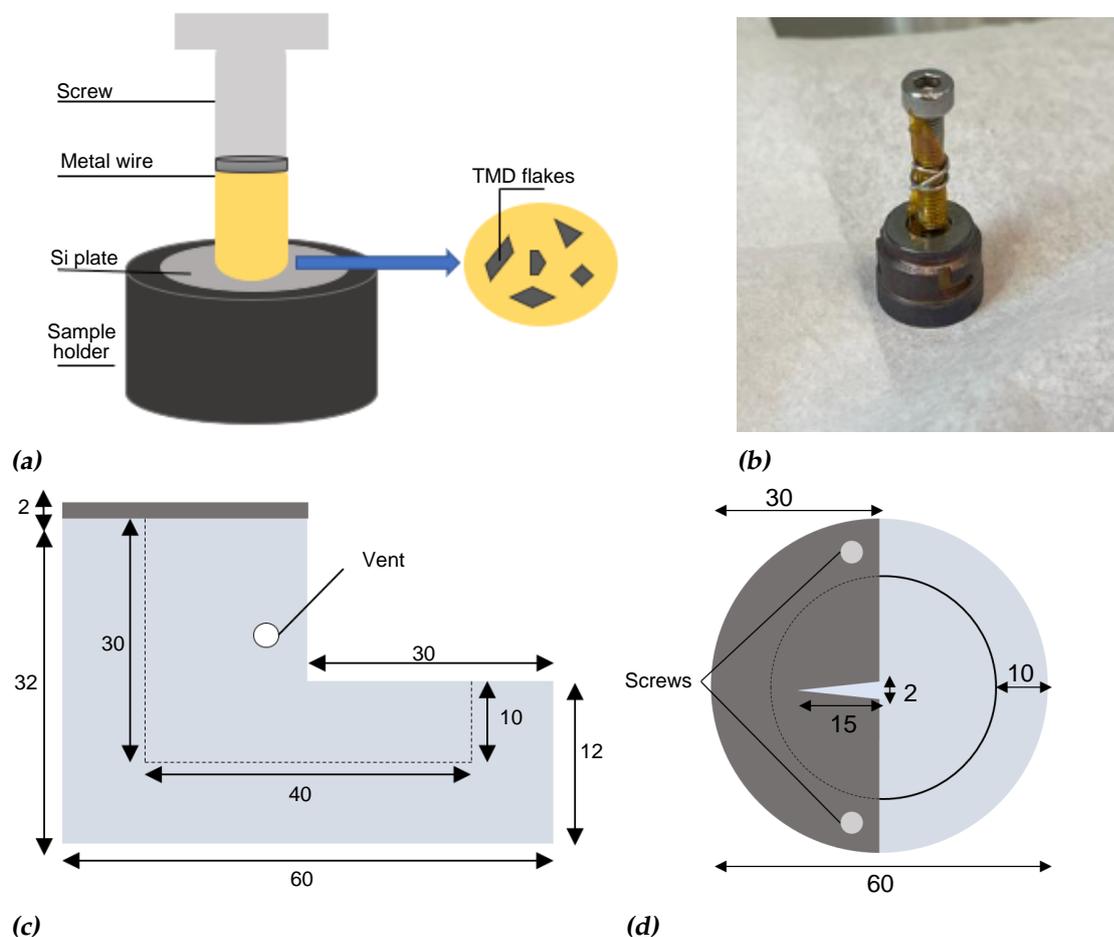
Figure 3.2: *The set-up and materials needed for in situ exfoliation in the load lock.* **(a):** *Schematic of screw, Kapton tape and sample cap. Zoom in: on back end of screw is tape with TMD flakes on it.* **(b):** *Screw with tape, positioned on sample holder. Sticky side is exposed to air.* **(c), (d):** *Side and top view of the tool respectively, dimensions in mm.*

tool, which schematics are shown in figure 3.2c,d. The vent seen in figure 3.2b protects against virtual leakage. Figure 3.2d shows that a metal plate is attached on top of the cup shape. The V-groove in this plate catches the screwhead.

With this method, we assume that with knocking off the screw, the last exfoliation step takes place in the load lock. The flakes that we image in LEEM are then cleaved in vacuum. Hereby we assume that Kapton's tape sticking force is larger than the force between layers, and a smaller than the force between substrate and first TMD layer. The proof-of-concept measurement was verified

with PEEM intensity and IV measurement of an MoS_2 sample. The next measurements are performed with $NbSe_2$.

3.3   Oxidation of $NbSe_2$ in the LEEM

The in situ exfoliated samples are measured after heating the sample up to 500-600 °C to remove contamination such as tape residue on the substrate. An oxygen gas line was added to the LEEM set-up such that we can add oxygen to the sample chamber consistently and at a controlled pressure (by opening or closing the needle valve more). The maximum oxygen pressure is constrained by the maximum sample pressure which is around 1e-6 mbar. To compare, we take measurements before and after the oxidation. Furthermore, we vent the sample in the load lock to investigate the difference in oxidation process between pure oxygen and air.

3.3.1   Overview of samples

To compare the in situ exfoliated $NbSe_2$, we also measure scotch tape exfoliated $NbSe_2$ in the LEEM. In table 3.1, an overview is given of the different samples that we measured in the LEEM.

Table 3.1: Overview of the samples measured in the LEEM: the material, exfoliation method and oxidation method. The order of oxidizing is as stated in the table.

	Material	Exfoliation method	Oxidation method
Sample 1	Mos_2	In situ	-
Sample 2	$NbSe_2$	In situ	Add oxygen
Sample 3	$NbSe_2$	Ex situ	1. Add oxygen 2. Vent load lock
Sample 4	$NbSe_2$	In situ	Vent load lock

3.4   Determining state of oxidation from LEEM data

We measure reflected intensity versus voltage curves i.e. IV curves to investigate whether the curves change upon adding oxygen. The Python package Napari is used to select a region to measure intensity. Besides the IV analysis,

we use additional (analysis) techniques to determine the oxidation state of the flakes.

3.4.1 Scanning Electron Microscopy and Energy Dispersive X-ray analysis

With Scanning Electron Microscopy (SEM) we have performed Energy Dispersive X-ray (EDX) analysis. With EDX, an electron beam hits the sample, which excites an electron from the inner shell. An electron from the outer shell falls back and releases energy in the form of X-ray radiation. As the energy difference is element specific, we can identify the elemental composition with EDX [37]. From the position on the energy axis of an EDX spectrum, we learn which elements are in our sample. We used the ThermoFisher Apreo SEM and used 8 kV electrons with normal incidence. We analyzed a $NbSe_2$ on Si sample after adding oxygen and expect to find Niobium, Selenide, Silicon, Oxide and Carbon (i.e. tape residue). All these elements have an X-ray peak below 8 kV. The data analysis is based on the code provided in [38], with some adjustments tailored to our data. Besides plotting the peak intensity of the components, we calculate the percentages of elements along the linecut. Also, the ratios between elements are computed.

3.4.2 Atomic Force Microscopy

Atomic Force Microscopy (AFM) is a technique used to characterize surfaces. We used tapping mode AFM (JPK Nanowizard 3), with a 70 kHz frequency tip. The sample surface is scanned with a sharp tip, mounted to a cantilever which vibrates close to resonance frequency. Due to sample-tip interactions, the oscillation of the tip varies. The height is adjusted according to the feedback based on this oscillation. This way, we measure height with sub-nanometer accuracy [39]. Also the phase difference between the drive and response is measured. A change in this phase lag indicates a change of material, which enables us to distinguish different types of materials with phase imaging. The square AFM images have sizes of 1 - 100 μm^2. Data analysis is performed with Gwyddion. The background is substracted with a line-by-line linear fit. Also, the color contrast in images is optimized. The minimal height value is set to zero.

We use AFM to characterize the roughness and height of flakes obtained with the new in situ exfoliation method. For the oxidation experiment, we use AFM as an additional tool: intensity contrast in LEEM in a certain flake cluster can be analyzed with AFM. Oxidation is expected to change the height profile of the

sample, as discussed in section 2.4.

3.5   Extra analysis techniques

3.5.1   Surface roughness

We analyze the surface roughness on flakes the LEED (Low Energy Electron Diffraction) pattern, according to the method reported in [40]. A perfectly flat surface would produce a sharp round (0,0) LEED spot. Roughness on the surface cause this spot to broaden. We take a linecut through the (0,0) LEED spot perpendicular to the dispersive direction of the magnetic prisms (see figure 3.1). The width of the peak i.e. FWHM is computed, which quantifies the in-plane momentum spread Δk. The width $\Delta \theta$ is then defined as:

$$\Delta \theta = \frac{\Delta k}{\sqrt{2m_e E_k}} \tag{3.5}$$

where $\Delta \theta$ is the deviation from the surface normal and $\sqrt{2m_e E_k}$ the total momentum [40]. If the same energy is chosen to compare line profiles, equation 3.5 simplifies to $\Delta \theta \sim \Delta k$.

We expect that oxidation changes the surface roughness. Namely, the resulting oxide layer is amorphous which is more rough than the original flake's surface. Therefore, surface roughness analysis yields us additional information about the oxidation state.

3.5.2   Principal Component Analysis

Principal Component Analysis (PCA) is a mathematical procedure used to reduce the dimensionality of data. The application of PCA to LEEM spectra is described in [34]. Regular analysis of LEEM images is to record images at different energies in real space or diffraction space. The data is interpreted as a set of images and in each image, intensity can be calculated to yield information about the electronic structure. Alternatively, the data can be represented as a vector in a multidimensional space [34] (instead of a set of images). Subsequently, the vector is projected to a lower-dimensional vector space, which is spanned by orthogonal PCA eigenvectors i.e. the principal components (PCs). The PCs represent the axes of the multidimensional space. These PCs are ranked according to the variance in the data they explain. With a determined number of PCs, the data is reconstructed.

For this analysis, we use the code in supplementary information of [34]. The PCA method is based on Singular Value Decomposition but we do not execute this full procedure with automated iterative PCA. First, we determine the suitable amount of PCs via a scree plot, which displays the number of PCs versus the cumulative percentage of data they describe. The PCs are established and due to the dimensionality reduction, the data can be clustered. Separate clusters represent different areas on the sample. The output is a color map, visualizing the different clusters on the sample. The IV spectra of these clusters are plotted separately.

The PCA method enables to identify different numbers of graphene layers and stacking domains in [34]. Consequently, we anticipate to reveal intact and oxidized areas of the sample with PCA.

Chapter 4

Results and Discussion

The main object of study was the oxidation of Transition Metal Dichalcogenide niobium diselenide $NbSe_2$. First, the *in situ* exfoliation method as described in section 3.2, is verified. Then, we proceed with the LEEM measurements of *in situ* cleaved $NbSe_2$ and expose the sample to pure oxygen. Subsequently, a study of $NbSe_2$ exfoliated in air is presented. Starting from LEEM images we continued the study with the (analysis) techniques described in sections 3.4.1, 3.4.2, 3.5.1 and 3.5.2. Finally, the difference of exposure to oxygen and air is examined.

4.1   Proof of concept measurement MoS_2

This measurement was performed to test the *in situ* exfoliation method as described in section 3.2. We used molybdenum disulfide MoS_2 as this has been extensively studied in the group, such that we know which features to expect in our measurement.

In the LEEM images, we observed MoS_2 flakes. Figure 4.1 shows the measured reflectivity versus energy, i.e., an IV curve of a flake recorded in real space. In figure 4.1 we observe the features characteristic for MoS_2. Specifically, the first state is located around 1 eV and the interlayer state is present at 5 eV [17, 20]. In figure 4.1, we observe a maximum around 20 eV, when the first order diffraction spot appears [20]. Here, we conclude we can do detect oxidation damage which was hypothesized: bulk MoS_2 is stable in air for these measurement periods. We have verified with the new *in situ* exfoliation method, a sufficient amount of flakes is transferred from the Kapton tape to the clean silicon substrate to
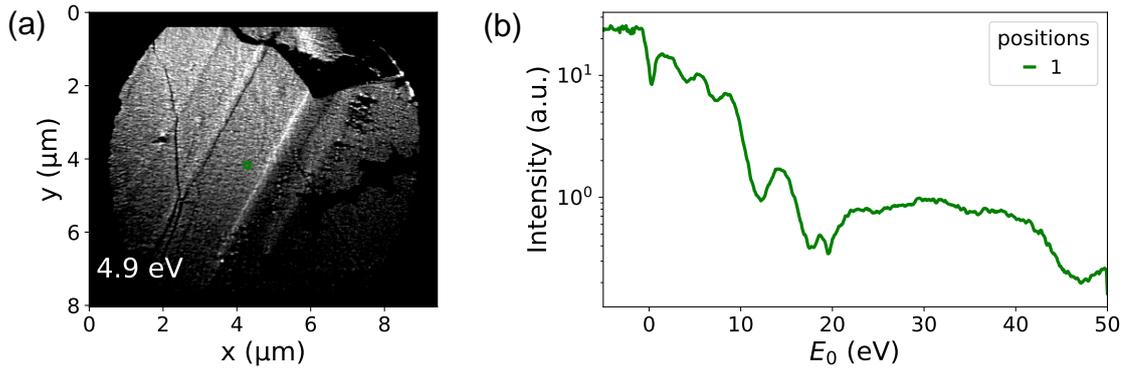
Figure 4.1: (a): *A real space Bright Field image of an MoS$_2$ flake, at 4.9 eV.* **(b)**: *Recorded reflectivity intensity for different energies, i.e., an IV curve of MoS$_2$, at the location with green marker (in the middle of figure 4.1a. Measured in real space.*

measure with the LEEM. Therefore we move on to our oxidation experiment.

4.2   Measurement of *in situ* exfoliated NbSe$_2$.

From now on, we measure NbSe$_2$ because we want to study the oxidation. Our hypothesis is that we can follow the oxidation process in bulk NbSe, better than in MoS$_2$ [22]. Here, we discuss the findings of sample 2: *in situ* cleaved NbSe$_2$ (see section 3.3.1 for a description of the samples).

The samples were heated to remove contamination (like tape residue) and IV curves were recorded. We perform μ-LEED with which we illuminate a smaller sample area, such that the diffraction pattern entails local information (described in section 3.1.1. The illumination aperture used is approximately 1 µm. Figure 4.2 shows an IV measurement of the (0,0) LEED spot in the diffraction pattern. The curve was corrected with the method described in section 3.1.2. In appendix A.1, the end result and regular average are compared in figure A.1, to show the improvement due to noise reduction. This improve is determined to be roughly 8 %.

The reflectivity of NbSe$_2$ at low energy is less studied than MoS$_2$. To validate our results, we compare the measure reflectivity R with the theoretical transmission T of NbSe$_2$, visible in figure 3 in [41]. Namely, $1 - T$ is the best approximation of R, if we neglect absorption. The energy axis in [41] shifted by the work function Φ, to align the zero energy in LEEM measurements (see figure 2.7 in section 2.3.2). Figure 4.2 shows the theoretical 1 - T in black and the experimental re-
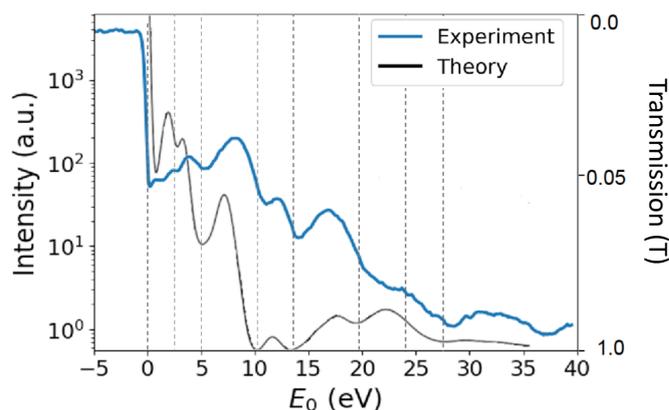
Figure 4.2: *Diffraction IV curve of sample 2: NbSe$_2$, cleaved in situ. Black curve: 1 - T with T the theoretical transmission, modified from [41]. The 1 - T values are plotted on the right y-axis. Dotted verticals mark theoretical reflectivity minima, i.e., presence of states. A great correspondence can be observed between experiment and theory, especially at lower energies ($E_0 < 15$ eV).*

sults in blue. The vertical dotted grey lines are a guide, and help to identify the reflectivity minima, which mark the locations of the states.

First we note that the intensities in figure 4.2 could not be normalized (as digital data was not available), therefore we cannot compare qualitative intensity values.

In general, we observe a good correspondence between the two curves: the first three experimental minima align excellent with theory. The states around 10 and 13.5 eV, are both shifted to slightly higher energy in our experiment. The theoretical minima are however sharper for the low energies. It is not likely that this shift is caused by inelastic scattering, as the measurement was performed with an illumination aperture. Electrons with lower energy then end up outside the aperture. Therefore, we attribute these slight shifts to contamination on the sample. Contamination can lower the work function, resulting in electrons that have a slightly higher energy. At higher energies, the curves in figure 4.2 match less: we observe a kink in the our experimental results around 20 eV, for which we would expect a minimum. At this energy, the first order LEED spots appear, which are not included in our measurement as the contrast aperture (visible in figure 3.1) only selects the specularly reflected electrons. As a result, we do not see the minimum, which is already not pronounced in theoretical curve, in figure 4.2.

4.2.1 Oxidizing the NbSe$_2$

We did a successful measurement on *in situ* cleaved NbSe$_2$, thus we proceed with the next step: oxidizing the sample. There is an oxygen line attached to the sample chamber of the LEEM which we use to to expose the sample to pure oxygen. We apply the maximum oxygen pressure of 1e-6 mbar, at a temperature of 360 °C, over a time period of roughly 30 minutes. With inspection of LEEM images, we did not observe differences in intensity or intensity contrast regions on the flakes. A diffraction IV curve measured after this exposure, is depicted in figure A.3 in appendix A.2. From this, we learn that 1e-6 mbar oxygen pressure is not sufficient to oxidize *in situ* exfoliated NbSe$_2$ flakes.

4.2.2 AFM characterization of flakes obtained by *in situ* exfoliation

The *in situ* exfoliation method is new and therefore we characterize the flakes obtained by this method with AFM. In general, the flakes are thick and vary in height from 80 - 150 nm. An example of AFM analysis on a flake of sample 2 is provided in appendix A.3. The surface roughness upon zooming in depends highly on the morphology of the flake, and is in this case circa 3 nm. The roughness on the flake is examined because in LEEM measurements, a surface should be as flat as possible. Then, the observed intensity contrasts dominantly indicate structural changes or different band structure.

4.3 Comparison to *ex situ* exfoliated NbSe$_2$

The *in situ* cleaved flakes that we discussed so far, did not exhibit any signs of oxidation damage. Therefore, we continue our research with a NbSe$_2$ sample that we cleaved *ex situ*. This means that all exfoliation steps were undertaken outside of the LEEM, such that the flakes were exposed to air before the LEEM measurements. We were motivated by previous LEEM data indicating that some boundary forms if NbSe$_2$ flakes degrade due to oxidation (see figure B.1). It is common to observe areas of different intensity in LEEM, but this boundary seemed unsharp, unlike areas we observe in TMD flakes. For illustration of typical sharp TMD features on flakes, see figure 2.4 or the sharp edges on the flake in figure A.4.

Remarkably, some NbSe$_2$ *ex situ* exfoliated flakes exhibited the same behaviour, which we did not observe for the *in situ* exfoliated NbSe$_2$ sample. An example is provided in figure 4.3a. Additional examples are provided in appendix A.1.1.
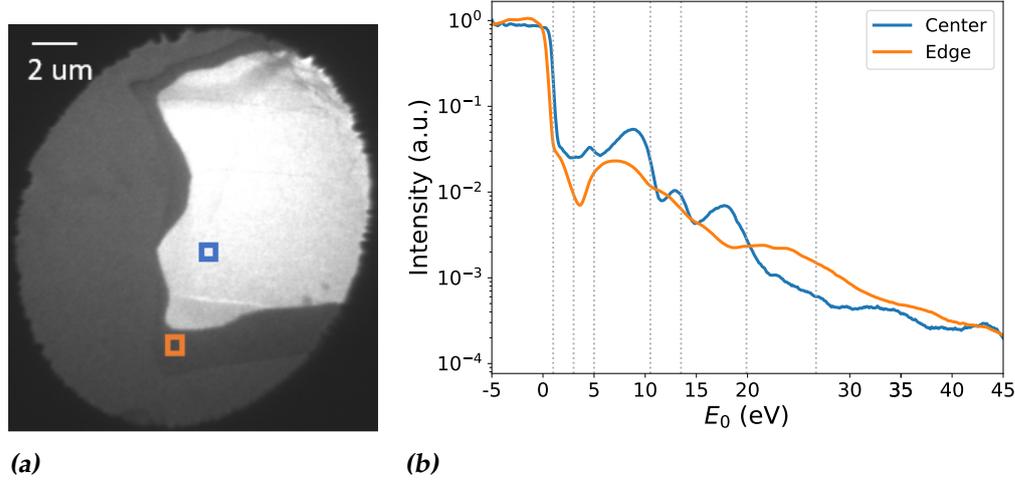
(a)   *(b)*

Figure 4.3: (a): *A LEEM Bright Field image of ex situ exfoliated NbSe₂ at 4.7 eV. We observe a flake with peculiar intensity boundary: high intensity in center and lower intensity around the edges. The boundary is not 'sharp', as commonly-seen in TMD flakes (see figure 2.4 for an example).* **(b)**: *Reflected intensity versus energy, recorded at the (0,0) LEED spot at the center and edge of the flake. The locations at which we measure the LEED pattern are indicated with blue (center) and orange (edge) in figure 4.3a. A clear difference is observed between the two IV curves.*

To highlight, the boundary was visible in the BF LEEM images around 4 or 5 eV consistently.

The intensity contrast in figure B.1 indicated that the flake could have undergone a structural change. We hypothesized that oxidation led to this boundary, as the difference between center and edge suggests a diffusive process, where a gas diffuses from the edges into the material [26, 30, 32]. The areas of high and low intensity are consistent: a high intensity region in the center, and a lower intensity region at the edges. This could imply that the center is intact while the edge, more prone to oxidation, is oxidized.

We conducted a μ-LEED measurement (as described in section 3.1.1), to investigate the LEED pattern at locations marked in figure 4.3. Curiously, the first order LEED spots are not visible at the flake's edge, while the center area does show the spots. This is shown in figure 4.4 below. The absence of diffraction spots can be caused by contamination or a very rough surface, which then masks the diffraction pattern. However, it could be also be an indicator of amorphous oxide [26, 29, 30]. We analyze the reflectivity versus energy (IV measurement) at the edge and center.
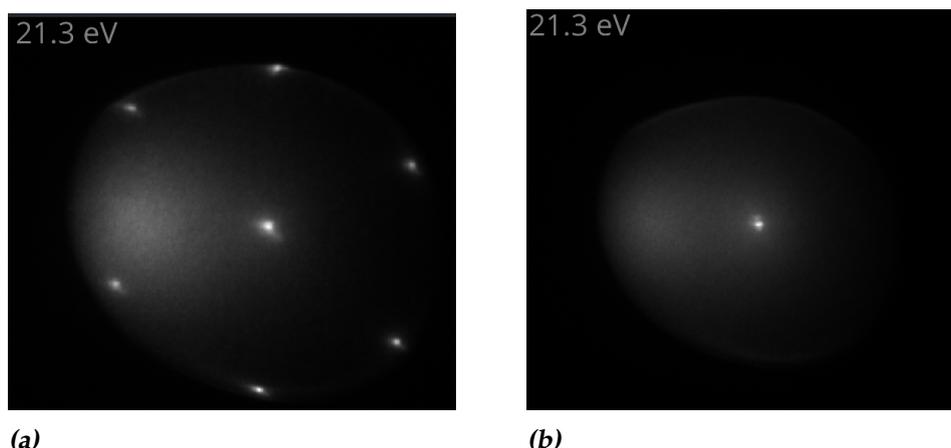
(a)   **(b)**

Figure 4.4: *Low Energy Electron Diffraction (LEED) pattern at 21.3 eV.* ***(a)****: Center area of the flake from figure 4.3a.* ***(b)****: Edge area of the flake from figure 4.3a. Here, the first order spots are absent.*

Figure 4.3b shows diffraction IV curves for two spots on the center and edge respectively. The result is remarkable: from figure 4.3b, it is clear that the electronic structure is different. The center IV curve resembles figure 4.2, with for example the difference that in figure 4.3b, the state at 3 eV is not present and the states at higher energy are hardly noticeable. The edge's IV curve exhibits different features: only one sharper, V-shaped minimum around 4 eV and from then, not any pronounced feature. This V-shaped minimum coincides with the energy at which we observe the intensity boundary.

With inspection of figure 4.3b, we hypothesize the underlying reasons for this distinct electronic structure. The sharpening of the reflectivity minimum visible in figure 4.3b indicates that the band structure changes. To see how, we turn back to figure 2.2b in section 2.1. A more pronounced minimum indicates that the two bands in figure 2.2b in the out-of-plane band structure, lie closer to each other. This causes the reflectivity minimum to be more sharp.

The absence of reflectivity minima for the higher energies can have multiple reasons. First, contamination like tape residue on the sample could break the interference effects, which results in the loss of interference peaks. Alternatively, the edge is a mix of oxidized and non-oxidized areas. If Nb_2O_5 is formed upon exposure to air, we anticipate the oxidized area to be a few nm higher than the intact area [25, 27, 28]. Namely, either an oxidized layer forms on top or oxidation takes place between TMD layers and thereby pushes up the lay-

ers on top. Consequently, the sample surface exhibits areas of different height. Then, electron waves that scatter on the intact areas and electron waves reflecting on oxidized areas have different phases, which again masks the interference extrema.

Exposure to pure oxygen and air

To examine whether the contrast edge moves, we expose it to pure oxygen again and subsequently to air by venting the sample in the load lock. The hypothesis is that the low intensity region grows as more oxygen is added. From section 2.4 it is known that humidity may play a role [31], hence we test both pure oxygen and air (which contains water). Important to note is that first, we add pure oxygen and later, the sample is vented in the load lock. We analyze the IV curves over time at the marked spots depicted in figure 4.5a. The results are shown in figure 4.5b.
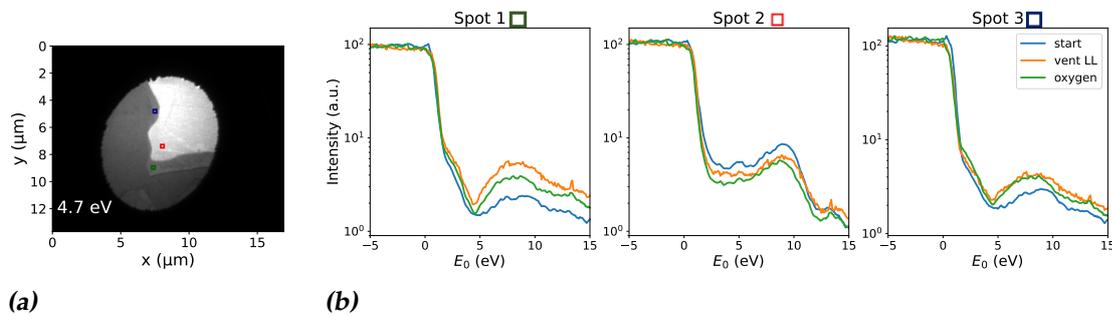

(a) **(b)**

Figure 4.5: (a): *Bright Field image of a NbSe$_2$ flake at 4.7 eV, where an intensity boundary between center and edge is visible.* **(b)**: *Real space IV curves, showing reflectivity at the marked spots on the flake in* **(a)**, *at different energies. Over time, the sample is first subjected to oxygen and then to air. The development of the IV curves at spot 1 and 3 is striking.*

Figure 4.5b reveals interesting insights: the reflectivity minimum of spot 1 and spot 3 sharpen over time. Here, we see the V-shaped minimum in figure 4.3b developing over time in figure 4.5b. The effect of oxygen and air is the least prominent for spot 2 on the sample. This is attributed to the oxidation process, in which the oxygen is more likely to interact with the edges [26, 30, 32]. In the LEEM BF images, we did not observe any movement of the boundary. That makes sense if we assume that the velocity of the oxidation boundary would be very slow; think about 50 nm per hour, which is even with the enlarged LEEM view, hardly noticeable.

These results indicate that we can follow the change in electronic structure of *ex situ* exfoliated NbSe$_2$ upon adding (pure) oxygen. However, to draw conclusions we use additional techniques to research the flake of interest.

4.3.1   SEM and EDX analysis

We performed SEM and EDX to further investigate the intensity contrast visible in LEEM. Figure 4.6a shows a SEM image of the flake cluster which contains the flake in figure 4.5a (right bottom). The flake also exhibits an intensity contrast in figure 4.6a. For the EDX analysis, our goal was to identify the chemical components in the center and the edge. We took three linecuts through the intensity contrast observed in LEEM images. Linecut 1 on the flake depicted in figure 4.5a, is discussed in detail.
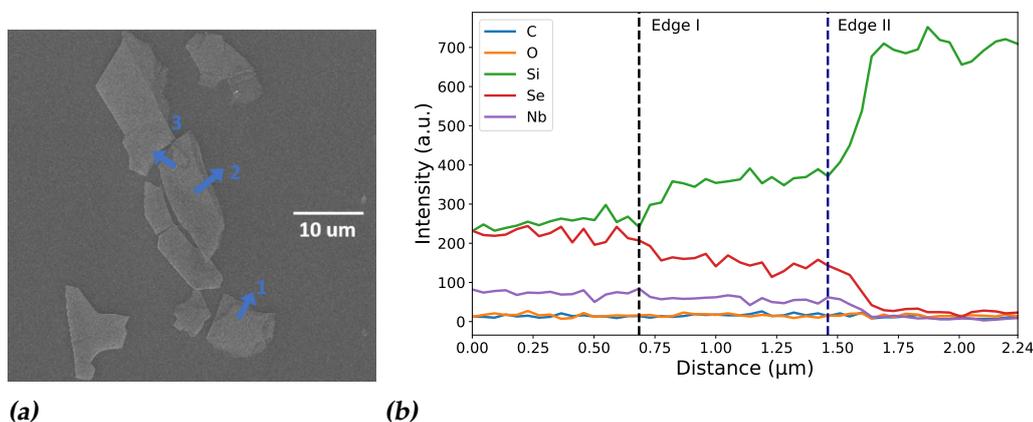

(a)   *(b)*

Figure 4.6: (a): *Scanning Electron Microscopy image of the flake cluster which entails the cluster in figure 4.5a. Blue arrows: the linecuts along which we assessed Energy Dispersive X-ray intensity.* ***(b)***: *Recorded EDX intensity along the linecut for the elements Nb, Se, Si, C and O. Black dotted vertical: edge I = high intensity - low intensity. Dark blue dotted vertical: edge II = sample - substrate.*

In figure 4.6b, the measured intensities for the elements niobium, selenide, silicon, carbon and oxygen are plotted. Two vertical dotted lines are visible in this plot. The black dotted line is edge I which is between the high- and low intensity regions. we define these regions as: region I corresponding to high intensity and region II to low intensity. The dark blue dotted line marks the edge between sample and substrate, called edge II. Figure 4.6b shows that at edge I, the Si intensity increases while the intensities of Nb and Se decrease. This indicates that the low intensity region is thinner, which leads to a larger part of

substrate (i.e., Si) intensity. We observe this more obviously at edge II, when the EDX intensities at the Si substrate are assessed.

In order to obtain insights into changes in chemical composition, we compute the mean value of the C and O percentage was computed, for region I and region II. The results are displayed in table 4.1.

Table 4.1: *Percentages of elements Carbon (C) and Oxygen (O) in different regions in the EDX linecut, visible as linecut 1 in figure 4.6a. We spot no significant difference in C and O percentages between region I and II.*

	% Carbon (C)	**C Intensity (a.u.)**	**% Oxygen (O)**	**Intensity O (a.u.)**
Region I	2.3 ± 0.5	14 ± 3	2.7 ± 0.7	16 ± 5
Region II	2.9 ± 0.6	17 ± 4	2.6 ± 0.6	16 ± 4

Table 4.1 demonstrates that the oxygen content is roughly equal between region I and II. This does not agree with our hypothesis that region II oxidized (and region I is intact), as this would result in a higher oxygen percentage. Also, there is no significant difference in carbon contamination which could explain the contrast we see in the LEEM and SEM and the absence of diffraction pattern. To note, is that oxygen and carbon are elements with low atomic mass for which EDX analysis is less accurate [42]. Namely, the X-ray yield of light elements is low and can be absorbed by the sample before being detected. Then, the EDX intensities do not reflect the true intensities of light elements. So our findings that the C nor O amount is different in regions I and II, are not conclusive.

Additionally, we calculate the Se/Nb ratio in both regions. Oxidation leads to the formation of Nb$_2$O$_5$, in which the Se atoms are replaced by oxygen. Then, we anticipate the Se/Nb ratio to be lower in an oxidized region. Alternatively, if we measure on an oxidized area where selenates have formed [25], the Se/Nb could spike. The ratios were 3.1 ± 0.3 and 2.7 ± 0.3 in region I and region II respectively. Thus, our analysis reveals no significant difference.

Figure 4.6a depicts two other linecuts which were consistent with the findings above. Hence, the EDX analysis does not indicate that the chemical composition in the sample is different in region I and II.

4.3.2 AFM analysis

With AFM, we have analyzed the flake of interest (of figure 4.3a). The height was determined to be around 90 nm. Furthermore, we evaluated the height

along a linecut through the intensity contrast observed in LEEM and SEM. The results are depicted in figure 4.7. The beam imprint from the EDX analysis line-
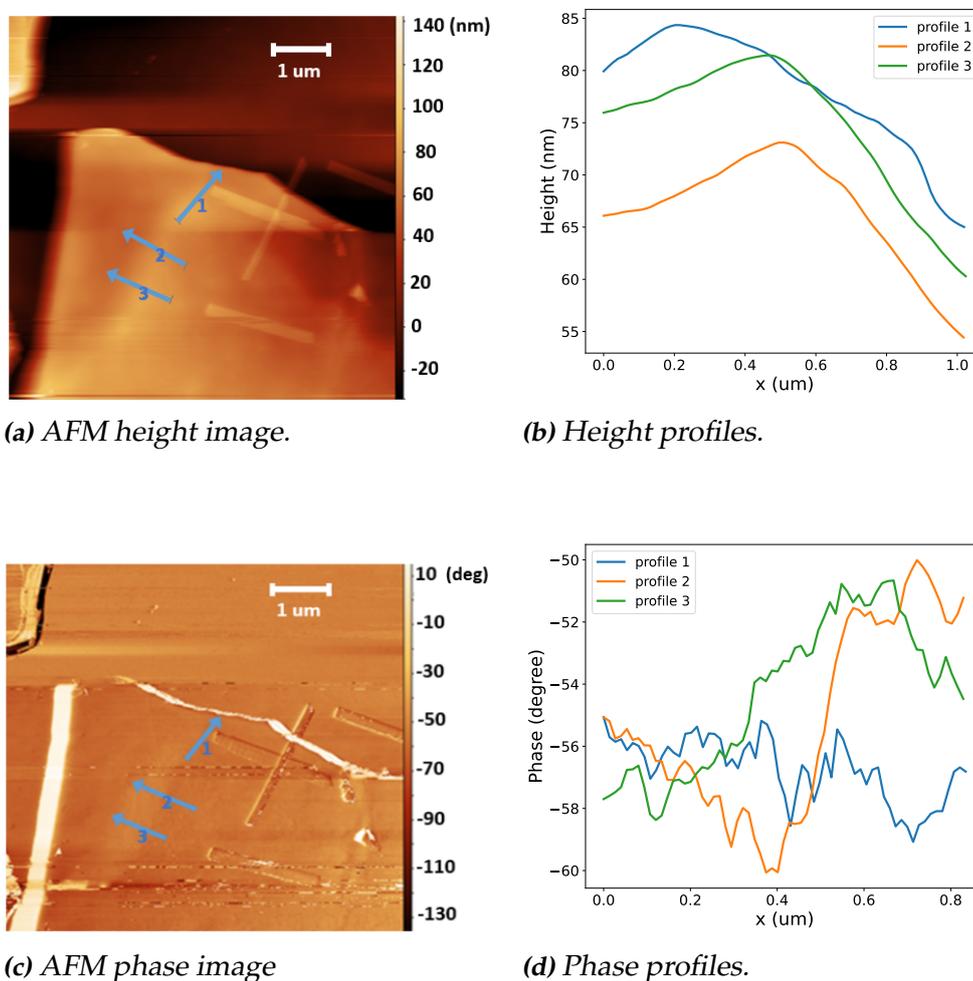

(a) AFM height image.

(b) Height profiles.

(c) AFM phase image

(d) Phase profiles.

Figure 4.7: *(a), (c): AFM height and phase measurements respectively (6.5 x 6.5 μm). The LEEM intensity contrast in the flake shown in figure 4.5a, is further studied. Blue arrows in (a), (c): along these linecuts, the line profiles are plotted, the direction is indicated. The linecuts cross the intensity contrast, supported by the EDX beam imprint visible in (a) (high intensity). (b), (d): Height and phase profiles respectively.*

cut, which is visible in figure 4.7a, helped to locate the AFM linecuts: the EDX trace crosses the high-low intensity contrast.

Figure 4.7b shows the height profiles, from which we determine that the height

difference between the center (A) and edge of the flake (B): A is 21 $\pm$ 2 nm higher than B. This result is surprising: (i) 21 nm is a large difference (circa 20 % of the thickness) and (ii) we did not expect the edge to be lower than the center. Namely, if a layer of Nb$_2$O$_5$ is formed at the edges, this oxide should increase the flake's height: reported values go up to a few nm [25, 27, 28]. The only outlier in the research stems from [29]: Budania et al. observed speckles after a long time period of exposure to ambient air, which could reach up to 0.1 µm, but this can be attributed to a longer measurement period of 1 year. The lower edge implies some effect that etches a part of the flake away. Another factor is the substrate which could react with the oxygen; Si can react with O$_2$ to form SiO$_2$. It is however highly unlikely that this reaction occurs, because the critical temperature ranges from 890 to 1150 °C and the critical pressure is between 7e-5 and 7e-2 mbar [43]. Both are high compared to our LEEM measurements with a maximum temperature of 600 °C and pressure 1e-6 mbar. Alternatively, this height contrast could occur at flakes that were mechanically damaged during the exfoliation process; then the origin of this boundary is not found in an interesting chemical or physical phenomenon taking place.

The AFM results do not support our hypothesis that the edges are oxidized. We did not find back any other flake which we measured in LEEM, as we have no opportunity to mark places of LEEM measurement. Therefore it is hard to give a statement about the height differences accompanying the irregular intensity contrast visible in 4.5a.

Determining roughness with LEED

Besides the AFM analysis of flakes, we can additionally execute a more local method, which uses the Low Energy Electron Diffraction (LEED) pattern. We have studied the surface roughness of the flake shown in figure 4.2a, according to the method clarified in section 3.5.1. A line profile through the (0,0) diffraction spot, perpendicular to the dispersive direction of the prisms in figure 3.1 is assessed. The width Δk, the in-plane momentum spread, yields information about the surface roughness at the location where the diffraction LEEM image is measured. We perform this analysis on the LEED data of the two locations visible in figure 4.2a. We found these were nearly identical. Figure B.4 presents the measured line profiles. Our hypothesis was that the roughness on the edge of the flake would be larger than in the center: Upon oxidation, amorphous Nb$_2$O$_5$ is formed [25, 26] (see also section 2.4) and this is expected to be more rough.

4.3.3 Optical microscope images of flake cluster

After the LEEM measurements, the flake cluster was imaged with the optical microscope, to. The goal was to investigate whether the boundary was visible under the optical microscope. The images are displayed in figure 4.8. The
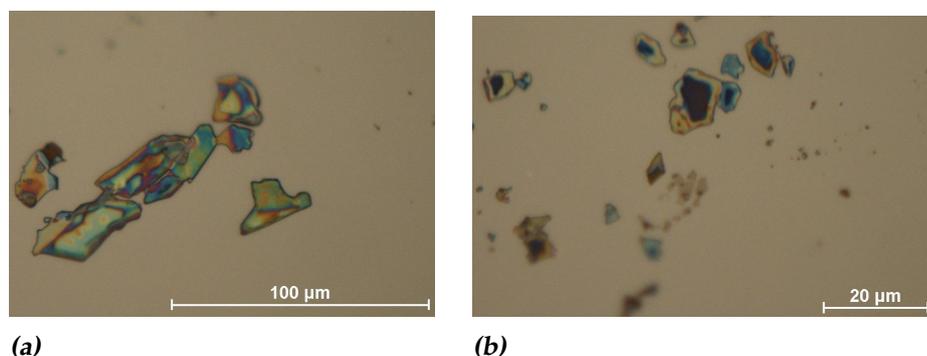

(a)   *(b)*

Figure 4.8: *Optical microscope images of ex situ exfoliated NbSe$_2$ flakes. **(a):** Flake cluster, including the flake in figure 4.5a. **(b):** Different flake cluster.*

wide range of colours shown visible in figure 4.8 is striking. Additionally, there seems to be different behaviour for the edges versus the center, in line with the previous LEEM measurements on the *ex situ* exfoliated LEEM flakes. It was researched whether these colours also occurred if NbSe$_2$ flakes on Si substrate are exposed to air (and without the high temperature in the LEEM). The results of this small experiment are described in appendix B.4. With the experiment, we conclude that features in figure 4.8 originate from the high temperature in the LEEM, as this sample was heated up to 600 °C.

4.3.4 Application of PCA to the LEEM data

The flake of interest in figure 4.5a has already been assessed with different methods like EDX and AFM. These results did not clarify the the origin of the boundary we observe between the flake's center and edge. Therefore, we proceed with an additional technique: Principal Component Analysis (PCA).

Section 3.5.2 described the implementation of PCA on LEEM data. The method is relevant for Bright Field (BF) and Dark Field (DF) LEEM images. We have applied the method for our BF data over time upon exposing the sample to oxygen and air subsequently. The PCA analysis thus serves as an additional analysis besides the IV analysis in 4.5b. The input for the PCA consists of one IV data set. We project the IV data to a lower dimensional space, spanned by orthogonal

eigenvectors, i.e., Principal Components (PCs). To optimize the analysis, the data is sliced in x- and y-direction such that we zoom in on the flake as much as possible, while retaining the edges of the flake. For clarity, we will now display all intermediate steps to obtain the clustered PCA image. To this end, the start data is used (before adding oxygen).

Figure 4.9a shows the scree plot, which displays the number of PCs and the cumulative percentage of data they explain. The scree plot has a characteristic
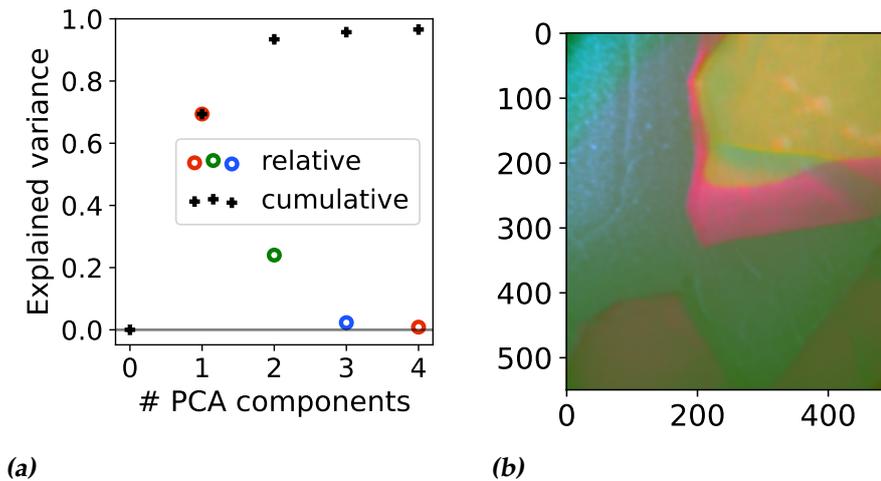

(a)   *(b)*

Figure 4.9: *First PCA steps on the flake of interest (see figure 4.5a). **(a)**: A scree plot, used to determine the suitable amount of PCs. **(b)**: A constructed Bright Field image, based on the first three PCs. The axes display the # pixels. Three PCs remarkably reproduce the features in figure 4.5a.*

'elbow' shape, and we select the number of PCs right before the curve flattens out. Figure 4.9a demonstrates that four PCs suffice as they explain 0.97 of the total variance. Subsequently, figure 4.9b shows the BF image that can be recreated with the first three PCs. When comparing figure 4.9b with figure 4.5a, we verify that the first three PCs accurately represent the data.

To cluster the data, the silhouette score can be utilized (see supplementary information of [34]). However, with this method, our data could be overfitted, implying that the number of clusters is larger than necessary. For example, if we want to distinguish between oxidized, not-oxidized and substrate, it will be sufficient to use three or four clusters. We tested both three and four clusters for each BF data set, and for the first two data sets (start and oxygen), the background is interpreted as two different clusters, hence a fourth cluster was used. The results are depicted in figure 4.10. Figures 4.10a depicts the first three PC
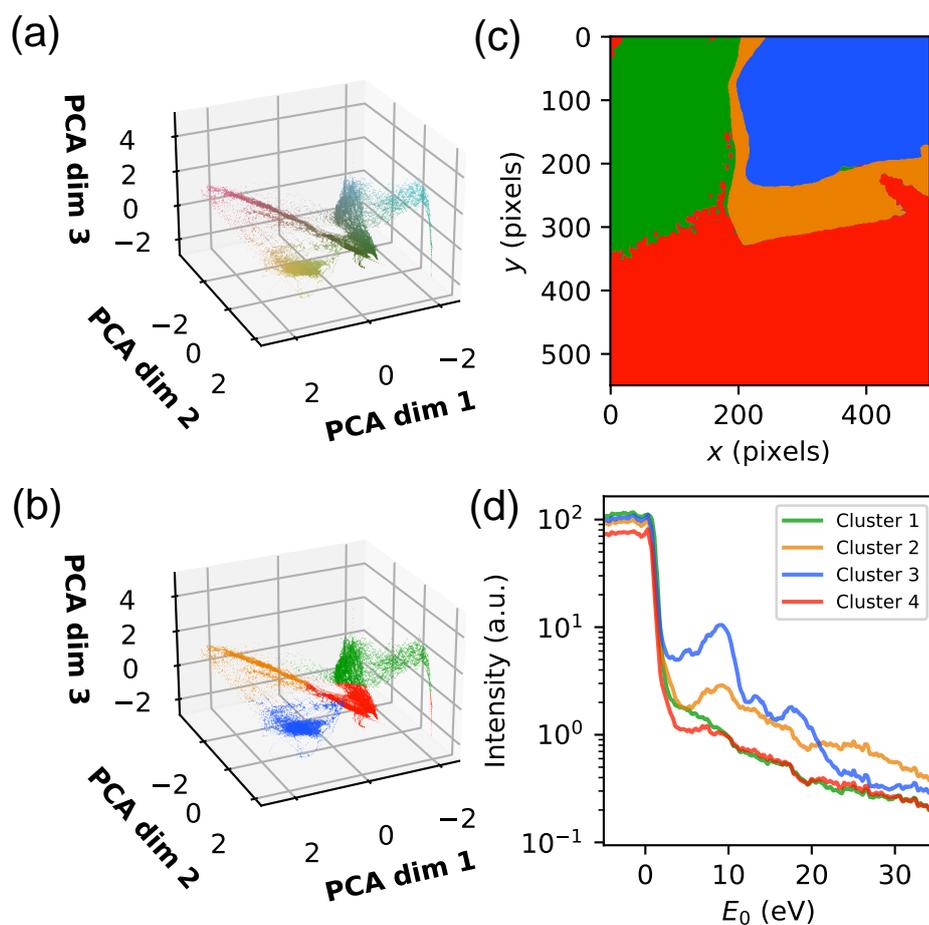
Figure 4.10: *Result of clustering of the PCs, from the LEEM data of the flake in figure 4.5a, before addition of oxygen.* **(a), (c)**: *Plot of the first three PC vectors used for clustering. We make use of four clusters.* **(b)**: *A reconstructed Bright Field image.* **(d)**: *IV curves of the clusters, which show a great correspondence with figure 4.5b.*

vectors, and and 4.10c again but then with the colours we will use for the clustered BF image. The clustered data represented as a BF image is shown in figure 4.10b. This image matches very well with the features we see in the LEEM image (see figure 4.5a). Additionally, figure 4.10d displays the IV curves of the clusters, which shows astonishing correspondence with the IV curves in figure 4.5b and 4.3b.

We note that indeed, the center (blue) is different than the edge (orange). The alternative PCA method excellently produces IV curves for the areas with assigned clusters. Particularly, the blue IV curve corresponds to the center's IV

curve shown in figure 4.5b: the two features at 3 and 8 eV are clearly visible. The red and green clusters indicate substrate: low intensity, absence of states. Interestingly, the flake, visible in figure 4.9b is not identified in figure 4.10d. This could be due to low intensity, which is masked as background.

Using PCA to follow oxidation

In the previous section, we have described the application of PCA and the analysis steps. The process was illustrated with the interesting flake's data before adding oxygen and air. We move on to applying PCA to obtain information about the oxidation state.

To this end, we carry out the analysis again, now on data after addition of oxygen. Figure 4.11 shows the results. Interestingly, figure 4.11a reveals the
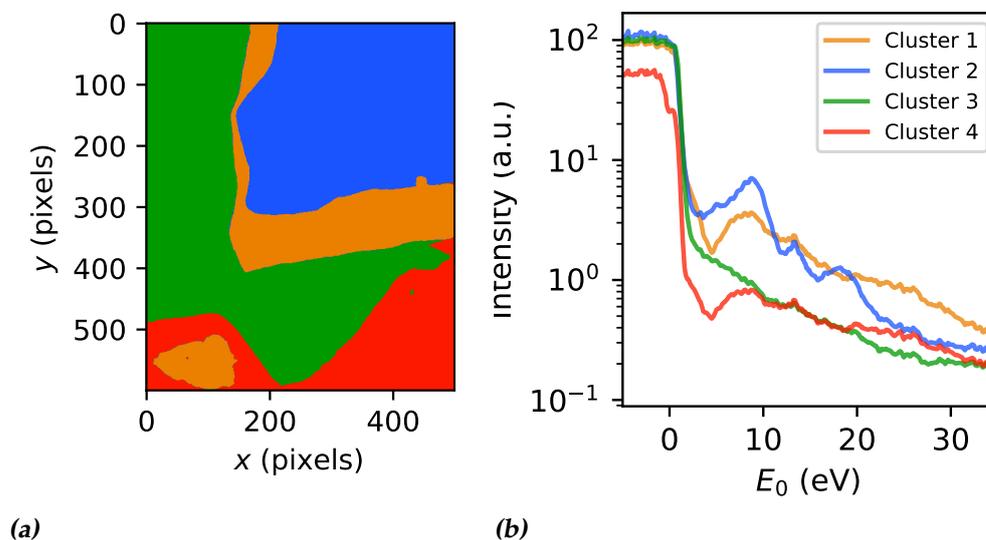

(a)   *(b)*

Figure 4.11: *Result of PCA on flake in figure 4.5a, after exposure to pure oxygen. **(a):** A reconstructed Bright Field image. **(b):** IV curves of the clusters. We see a new feature appearing with respect to figure 4.10b.*

development of a feature on the bottom flake. One could argue that cluster 1 is similar to cluster 4, but we do notice that the reflectivity minimum is more sharp for cluster 1. Additionally, the IV curve of cluster 1 resembles the IV curve at the flake's edge in figure 4.5 well. Therefore, the appearance of this feature in the PCA representation, can be an indicator that the bottom flake is oxidized upon adding oxygen. In section 4.2.1, we found out that 1e-6 mbar oxygen pressure is not enough to detect changes of a clean, i.e., *in situ* cleaved NbSe$_2$ sample in

the LEEM BF images or IV measurements. From the results presented in the paragraph above, we could conclude that 1e-6 mbar oxygen is sufficient if the sample has already been in contact with (pure) oxygen.

The analysis was repeated after venting the load lock. The results were consistent and are shown in the appendix B.3 in figure B.5. A slight difference is that the data is reconstructed with three clusters: this because the bottom flake in figure 4.5a is not in the LEEM measurement window. Consequently, we did not obtain further information about the development we observed in figure 4.11 with PCA on this data set.

We continue to study the resemblance of the IV curves reconstructed with PCA with the curves shown in figure 4.5b. Therefore, we plot the clusters in 4.11d over time, upon adding oxygen and air respectively. The results are visible in figure 4.12. Figure 4.12 demonstrates the similarity of the clusters found with
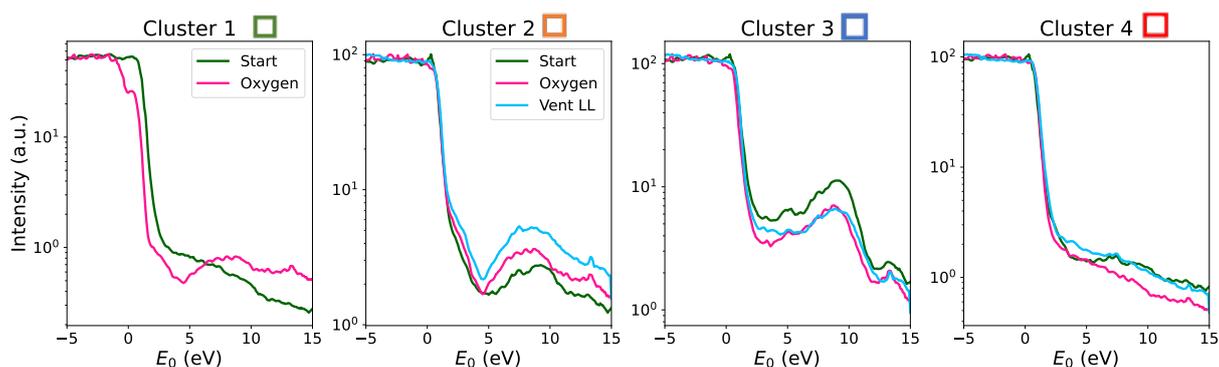

Figure 4.12: *Development of the IV curves of four clusters identified with PCA on the flake of figure 4.5a.*

PCA and the IV measurements at the spots indicated in figure 4.5a. Cluster 4 represents the substrate. Then, for the start sample, cluster 1 is identified as substrate while we see the development of the V-shaped minimum after adding oxygen. This shows more clear in cluster 2, which describes the edges of the flake while cluster 3 is formed by the flake's center. Again, the IV curve of the edge is more affected by the (pure) oxygen than the center, see section 4.3.

The alternative analysis technique, PCA, has shown to be corresponding to the results from IV measurements. Additionally, we discovered that performing PCA over time, we can follow the changes in electronic structure live.

4.4 Investigating the influence of air versus oxygen in oxidation

So far, we observed features that could be caused by oxidation exclusively on the sample, which was already exposed to air before loading it into the LEEM (see section 4.4 for the details). We saw peculiar intensity boundaries as well as a development of the first reflectivity minimum (visible in figure 4.5) upon addition of (pure oxygen). A clean, *in situ* cleaved, sample did not exhibit changes when it was exposed to pure oxygen (see section 4.2.1). This raises the question whether the combination of oxygen and water, present in air, is crucial for observing degradation due to oxidation. According to literature, humidity can play a decisive role in the oxidation process [29, 31]. Consequently, another *in situ* exfoliated sample was prepared, and only exposed to air, by venting the sample in the load lock.

4.4.1 Surface roughness analysis

We want to further test this analysis technique, hence we apply it to our new data. According to the method in section 3.5.1, the width of the line profile of the (0,0) LEED spot (perpendicular to the dispersive direction), provides a measure for surface roughness. We performed LEED measurements and examined the in-plane momentum spread Δk of the same flake, before and after venting the sample in the load lock. The spread was assessed at 19.2 eV and repeated for 22.4 eV, to verify consistency. The measurements were conducted at the center of the flake in figure 4.13a. At both energies the first order LEED spots are visible. The results are shown in figure 4.13. Figure 4.13 shows that Δk at the start is smaller than after venting in the load lock. Table 4.2 displays the computed FWHM values of the curves in figure 4.13.

Table 4.2: *Calculated FWHM values of the in-plane momentum spread Δk shown in figure 4.13. Here, the FWHM is an indication for surface roughness.*

	FWHM (in 1 / Å), E_0 = 19.2 eV	FWHM (in 1 / Å), E_0 = 22.4 eV
Start	0.20 ± 0.03	0.20 ± 0.05
Vent load lock	0.36 ± 0.04	0.46 ± 0.04

Figure 4.13 and table 4.2 imply that the flake's roughness at the start, is smaller than after it was in contact with air. This is in line with our expectation: upon oxidation a rougher amorphous oxide layer is formed, as reported in [26, 29, 30].

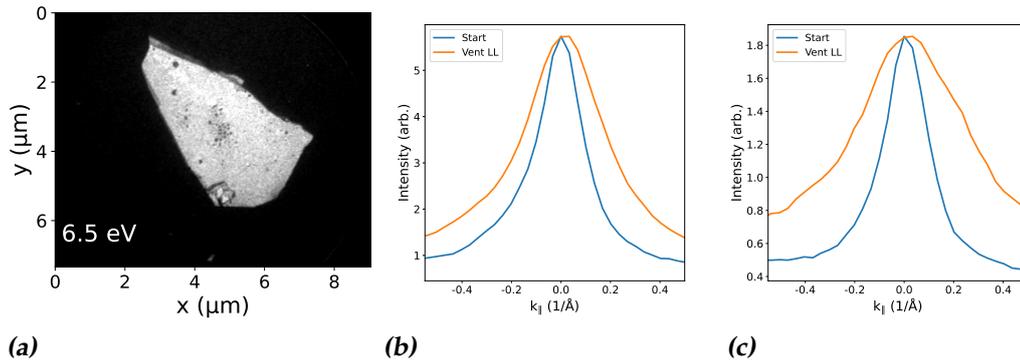From the roughness analysis, we would conclude that venting the sample in

(a)   *(b)*   *(c)*

Figure 4.13: (a)*: Bright Field LEEM image of in situ exfoliated NbSe$_2$, at 6.5 eV.* **(b)**, *textbf(c): Line profiles of the (0,0) LEED spot, perpendicular to dispersive direction of the magnetic prisms (see figure 3.1). The FWHM is a measure of surface roughness [40]. Measured at 19.2 eV. and 22.4 eV respectively.*

the load lock triggered some process to increase roughness, which could be attributed to oxidation. It should be noted though, that this analysis on its own can not verify that the flakes are oxidized. Namely, roughness can also increase if dust from the air settles on the sample. In the sample chamber, pressure is 1e-9 mbar, so most of it should be removed but even at this pressure some contamination is possible. Therefore, the roughness analysis should be used as an additional support, instead of a decisive measurement.

4.4.2   Evaluating the consistency of measurements

For the *in situ* LEEM measurements, we presumed that all flakes we observed were clean, as they were cleaved with the method treated in section 3.2. In this section, we examine the consistency of our method and the drawn conclusions about the intensity boundary in the NbSe$_2$ flakes (the details can be found in section 4.3). An example of a flake which seems to exhibit the same contrast is provided in figure 4.14a.

The flake in figure 4.14 seems to show the intensity boundary again with high intensity in the center and low in the edge area. In figure 4.14, the reflectivity versus energy is plotted for the spots marked in figure 4.14a. The IV curve at first sight resembles the curves visible in figure 4.3b. Upon closer inspection, we however see that the IV curve of the edge (red in figure 4.14b) does not show the V-shaped first reflectivity minimum, which was characteristic for the edge IV measurement (see also figure 4.5b). It appears that the edge's reflectivity behaves similarly to the background, as demonstrated in 4.10 in the green and red
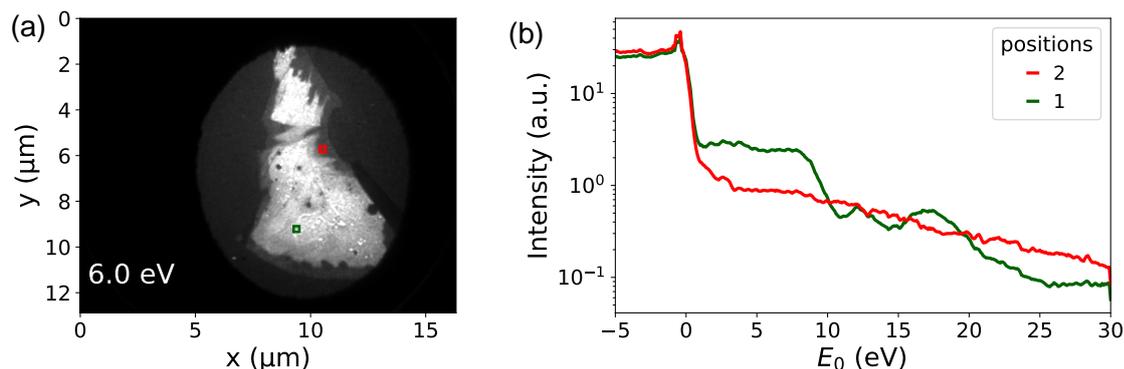
Figure 4.14: (a): *A real space Bright Field image of an in situ exfoliated NbSe₂ flake, at 6.0 eV. There seems to be an intensity contrast between center and edge (similar to 4.3b).* **(b)**: *Measured reflectivity intensity for different energies, i.e., an IV curve, at the spots marked* **(a)**. *Recorded in real space.*

curves. The low intensity at the edge of this flake is attributed to a contaminated surface. This is supported by the lack of states visible as reflectivity minima in figure 4.14b.

This example was shown to clarify the difference between (i) flakes like in figure 4.3a from which we believe that the boundary separates NbSe₂ with different electronic structure, and (ii), flakes that display an intensity contrast, from which we assume it is due to contamination (like tape residue).

After exposure to air, no flakes were discovered which exhibited the same IV behaviour as the *ex situ* exfoliated flakes. The IV measurements are shown in figure C.1. This supports the hypothesis that the flake was clean before, and the intensity boundary stems from contamination. For an oxidized flake's edge, we would namely expect the features described in section 4.3. With this, we propose that only flakes that are already degraded due to oxygen, will show more oxidation damage signs upon addition of (pure) oxygen.

Chapter 5

Conclusions and Outlook

5.1 Conclusions

In this research, we have developed a new method to exfoliate TMD flakes *in situ* in the Escher LEEM set-up. This method was implemented to investigate the oxidation process, for which we used bulk niobium diselenide, $NbSe_2$. The IV curves measured in diffraction space were corrected for electron gun noise, which improved the smoothness by 8 %.

In section 4.2, we assessed the flake's reflectivity versus energy, so-called IV measurements. These showed great correspondence to the theoretical prediction in [41]. Pure oxygen at a pressure of 1e-6 mbar (in a time period of 30 minutes), was not sufficient to observe changes in the LEEM images and IV measurements.

Interestingly, we have noticed the difference between exposure to pure oxygen and air in section 4.3: flakes exposed to air before conducting the first LEEM measurements, did show signs of degradation. Specifically, a boundary between edge and center with low and high intensity respectively was visible and the areas exhibited different IV curves. The first reflectivity minimum of the edge's IV curve exhibited a sharp V-shape (visible in figure 4.3). Upon addition of oxygen and air, the V-shape continued to sharpen over time. By eye, no changes in the BF LEEM images were observed. With the usage of PCA on this data, we have confirmed that PCA to accurately identifies these different areas in a BF LEEM image. Furthermore, the IV curves are excellently reproduced by the analysis. To conclude, with the LEEM IV measurements (in combination with PCA), we are able to follow the changes in band structure live. The change

of electronic properties is attributed to oxidation, as this was the variable factor in this experiment.

Further investigation into the origin of the intensity contrast was executed, but EDX and AFM did not give conclusive results. According to the EDX analysis, there was no significant difference in the Se/Nb ratio between the edge and center. This would be expected if the edge is oxidized and the center intact. From AFM, we learned that the center is 21 nm higher than the edge, which does not agree with literature findings of oxidized TMDs [25, 27, 28].

We have explored an additional technique besides AFM to examine the surface roughness via the (0,0) LEED pattern. Lastly, we explored whether a difference exists between oxidation in pure oxygen and air. We found that flakes that were already in contact with air, and therefore supposed to be degraded at time zero, are more prone to further degradation upon adding (pure) oxygen.

It is clear that further investigation is needed for a better understanding of the oxidation of bulk $NbSe_2$. Namely, TMDs are suitable candidates for the development of optoelectronic devices due to the indirect band gap in the visible light range [9].$NbSe_2$ specifically is interesting, as it was used to fabricate the first solid, conductive lubricant which is stable in vacuum, over a wide temperature range [44]. For the quality of the electronic devices, it is desirable that oxidative degradation is minimized [12].

5.2   Outlook

To obtain a definitive explanation on the features observed on the$NbSe_2$ flakes, we can use a different method to identify the elemental composition. Raman spectroscopy is suitable for this, due to its locality [45]. Raman spectroscopy measures the energy shift of inelastically scattered photons which are excited after incident light hits the sample [46]. As the wavelength shift is dependent on chemical composition of the scattering molecules, it is used for component identification. This technique was used before to analyze oxidation damage [29]: Budania et al. observed differences in Raman spectra of thin flakes between affected and intact areas.

The EDX analysis did not yield conclusions about the oxidation state. We propose an adjustment for EDX measurements on samples that are suspected to be oxidized. In particular, the beam incidence can be changed from normal to almost sheering incidence, to maximize the amount of measured oxygen. With our measurement, electron beam hit the sample at normal incidence such that the full thickness of sample is measured. The oxide layer is expected to be thin

compared to the full flake height. Therefore, with normal inciding beam, we expect a small part of the signal to be due to the oxide layer. In contrast, sheering incidence results in measurement of the top layer, which should lead to a larger percentage of oxygen.

Another suggestion for follow-up research is to repeat the oxidation experiments with thinner flakes. As discussed, the oxygen enters the material from the side and the top. In particular, the edges are more prone to react with oxygen [26, 30, 32]. We hypothesized in section 4.3.2, that the formed Nb_2O_5 could be located between layers and thereby push up the TMD surface. If the TMD flake is thinner, this height effect will be observed more easily [29]. A method to obtain thin flakes is to evaporate the substrate with a layer of gold (with a sticking layer of Nb or Cr) [47]. We have already tested this method, which yielded areas of thin flakes, which is reviewed in appendix D.

For future research into oxidation, it is desired to have longer measurement windows. During this project, we were subject to time constraints. Consequently, we did not measure flakes after 90 days or 1 year, similar to the approach in [28–31].

Before changing up the system, we need to further explore $NbSe_2$. Subsequently, though, a logical next step would be to perform the *in situ* exfoliation and oxidation with a different TMD. Accordingly, it is possible investigate whether the flakes of a different TMD exhibit similar intensity boundaries. As described in section 2.4, the electronegativity of the chalcogen (sulfide, selenium or tellurium) influences the oxidation. For S, Se and Te respectively, the bonds between the metal and oxygen are stronger. For example, $NbTe_2$ would be more prone to oxidation [48]. It should be noted, though, that for S, Se and Te, the amount of states increases [20], which could mean that states are more easily masked in the IV measurements. Also, the transition metal could be different, as for example tungsten disulfide and - diselenide (WS_2 and WSe_2) have already been objected to oxidation studies [23, 27, 28, 31].

Details about measurements of *in situ* exfoliated NbSe$_2$.

We now show additional results that support the results described in section 4.2. The noise reduction is quantified, and then details about the oxidation experiment are provided.

A.1 Quantification of noise reduction

Figure 4.2 shows an IV curve which was recorded from the (0,0) Low Energy Electron Diffraction (LEED) pattern. This spot is elongated because electrons have slightly different energies upon leaving the electron gun, see section 3.1.2 for details. The IV curve is corrected for this energy dispersion. Figure A.1a shows both the regular average (obtained by averaging over all pixels in the linecut) and the corrected average.

Visually, we observe that the corrected curve is smoother. To quantify this, a noise factor is computed. First, the average is divided by the corrected average and then the mean is subtracted to center the noise factor around zero. If we assume that the corrected average is a smoother and more correct version than the regular average, this noise factor indicates the percentual improvement by correcting. The noise factor is plotted in figure A.1b. The standard deviation of the factor provides the percentual improvement, which is 8 %.
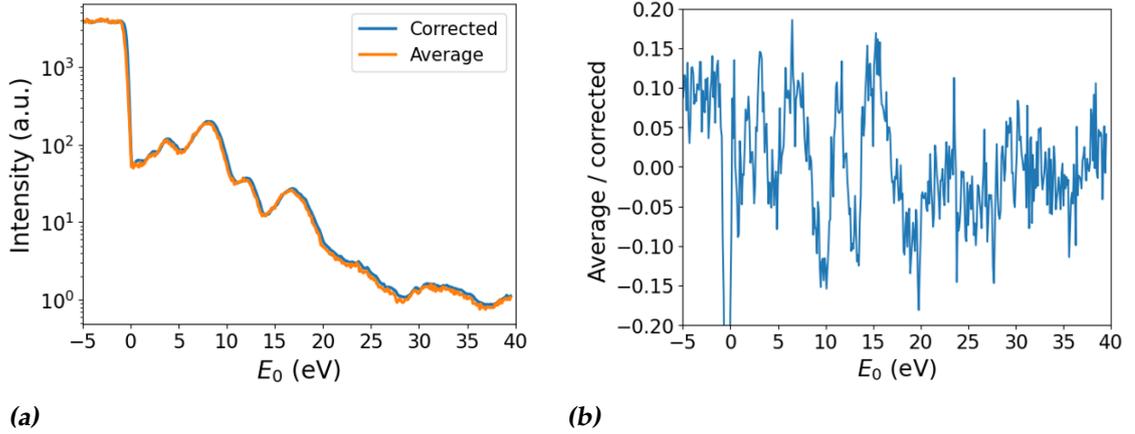
(a)   *(b)*

Figure A.1: *Quantification of improvement of the IV curve (measured in diffraction space), with noise reduction. **(a):** The average and corrected IV curves of sample 2: NbSe₂, cleaved in situ. **(b):** Plot of the noise factor = average / corrected. The mean subtracted to center the noise factor around 0. The standard deviation, 8 %, of this factor quantifies the improvement due to correction.*

A.1.1   Calculation of energy per pixel (in eV)

For the method described in section 3.1.2 we determine the correct energy per pixel (in eV) value, defined as δ. The calculation of δ was carried out in [35] for the setting 'diff hi' in the LEEM measurement. Now, we repeat the steps for 'diff std' to ensure that the correction described in section 3.1.2 is performed with a correct energy per pixel value. The method is described in [35] and makes use of the shift of the reflectivity minimum between frames. Namely, we know this minimum should appear at the same electron energy. The difference in energy is derived with a line profile through the (0,0) LEED spot. The linecut is taken parallel to the dispersive direction, which obtains us a spread in out-of-plane momentum. An example is shown in figure A.2.

In figure A.2 a minimum is visible in the Electron Energy Loss Spectroscopy (EELS) plot. The location of this dip shifts between frames, as seen in figure A.2. With this energy shift, ΔE_{shift}, and number of pixels, the energy per pixel (in eV) is computed. We determined:

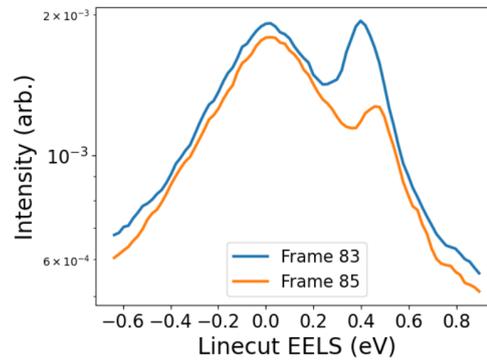$$\delta = \frac{\Delta E_{shift}}{\#pixels} = 0.033 \pm 0.001 \quad eV/pixel$$

Figure A.2: *The Electron Energy Loss on the x-axis is plotted against intensity of the (0,0) diffraction spot. The energy loss of electrons is correlated to the pixel location: this is how the elongated spot arises, which we discussed in section 3.1.2. The energy shift between the plotted frames determines the energy per pixel (in eV) for the 'diff std' setting of the LEEM set-up.*

A.2 Reflected intensity upon adding oxygen

We measured the reflectivity for *in situ* exfoliated NbSe$_2$ flakes. Now the oxidation experiment is implemented and pure oxygen is added to the sample, at temperature 360 °C and 1e-6 mbar pressure. We anticipated to observe changes in the LEEM images or IV curves. However, as shown in figure A.3, the IV measurement still matches well with the curve before adding oxygen (in figure 4.2). Also, no changes in the LEEM BF images were visible. From this figure, we
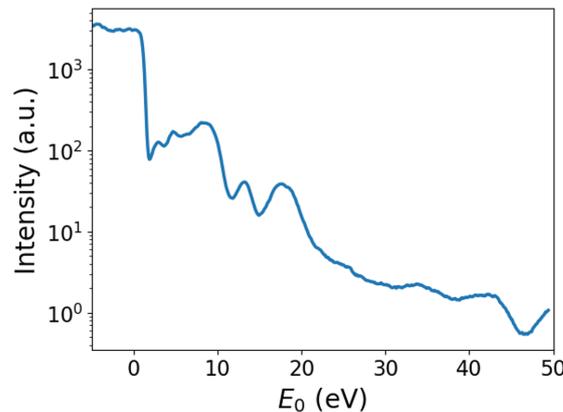

Figure A.3: *The reflectivity at different energies, measured on the same flake of which the (0,0) LEED spot is visible in figure 4.2. This IV curve was recorded after exposure to pure oxygen. The IV measurement before, is depicted in figure 4.2b.*

conclude that the amount of oxygen was not sufficient to follow the oxidation

degradation live.

A.3   AFM characterization of flakes

We have implemented a new exfoliation technique to cleave crystal in vacuum. In this section, the flakes are characterized with AFM analysis. Here, we provide examples of thickness of flakes and the surface roughness on the flakes.

Figure A.4 depicts a flake which clearly shows sharp edges that occur between different parts of the flake. This is caused by the exfoliation method, where some layers are ripped of while other stick to the Kapton tape. We take a line-
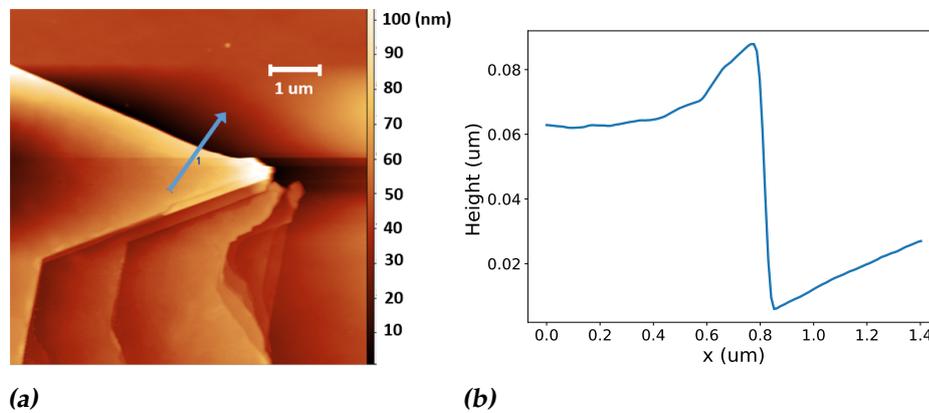

(a)   *(b)*

***Figure A.4: (a)**: Atomic Force Microscopy image of a flake in sample 2 (in situ exfoliated). We measure the height along the linecut shown in blue. **(b)**: Height profile along the linecut.*

cut from the edge of the flake to the substrate, which is visible in figure A.4a. This way, the flake's height is determined. From figure A.4b we learn that the height is roughly 80 nm.

To examine the roughness on the surface of the flake, we measure a zoomed-in area on the flake in figure A.4. Now, we randomly draw a linecut across the surface and analyze the height differences. The results are shown in figure A.5. In figure A.5 we notice that the height on the surface of the flake in figure A.4 fluctuates with approximately 3 nm. For LEEM measurements, we aim to obtain a surface as flat as possible, but a roughness of a few nm is acceptable.
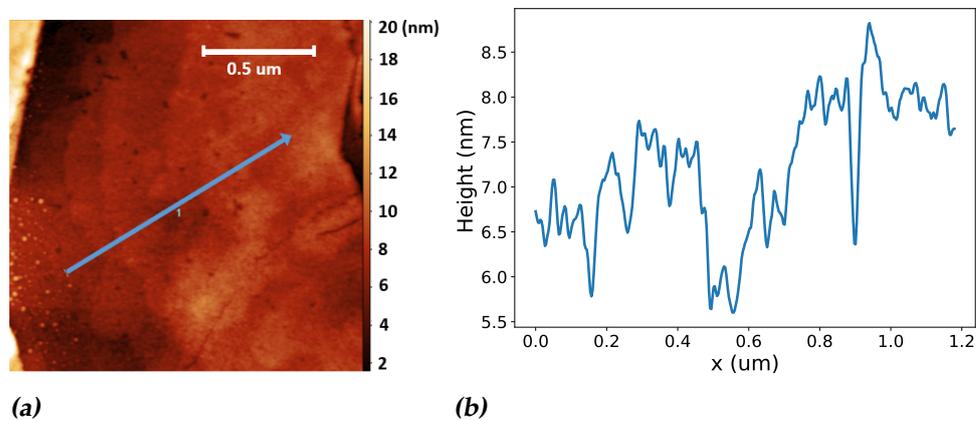
(a)   **(b)**

Figure A.5: (a)*: Atomic Force Microscopy image, selecting a small region on the flake shown in figure A.4. We measure the height fluctuations along the linecut shown in blue.* ***(b)****: Height profile along the linecut.*

B

Details about measurements of *ex situ* exfoliated NbSe$_2$.

This appendix treats additional results and analysis of sample 3, discusssed in section 4.3. These consist of (i) examples of an observed intensity boundary in flakes, (ii) roughness analysis and (iii) PCA.

B.1 Examples of intensity boundary in NbSe$_2$ flakes

We are investigating the oxidation and this started with interesting observations on NbSe$_2$ flakes some time ago. Figure B.1 shows an example, where an intensity boundary on the flake itself is visible. The center and edge exhibiting high and low intensity respectively. During the measurement of *ex situ* NbSe$_2$,
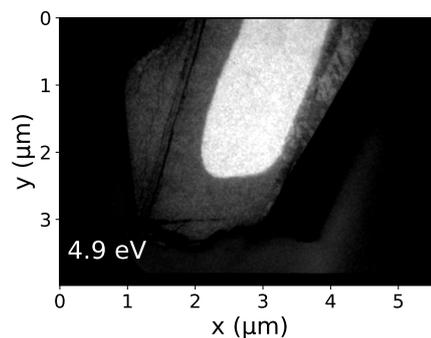

Figure B.1: *Bright Field image of a NbSe$_2$ flake at 4.9 eV, where an intensity boundary between center and edge is visible. Measurement stems from 2021.*

similar flakes were encountered. Figure 4.3a shows this intensity contrast. In figures B.2 and B.3 below, we provide additional examples.
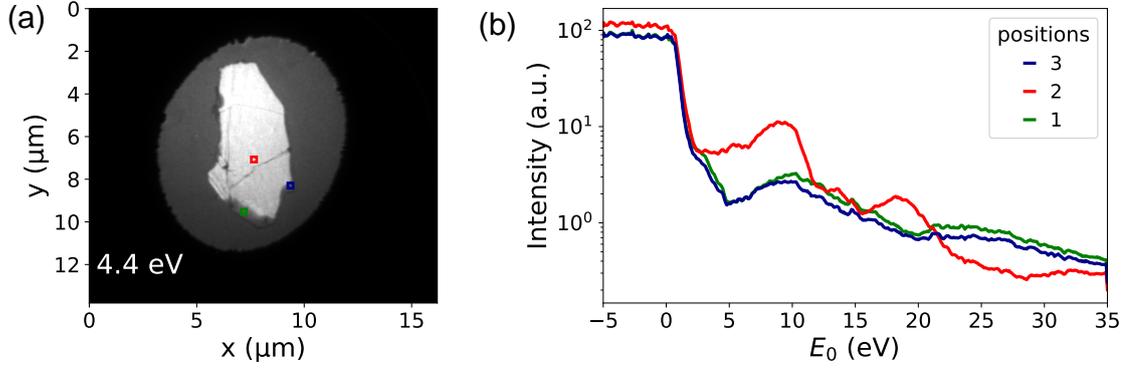

Figure B.2: (a): *Bright Field image of a NbSe₂ flake at 4.4 eV, where an intensity boundary between center and edge is visible.* **(b)**: *Real space IV curves, showing reflectivity at the marked spots on the flake in* **(a)**, *at different energies*
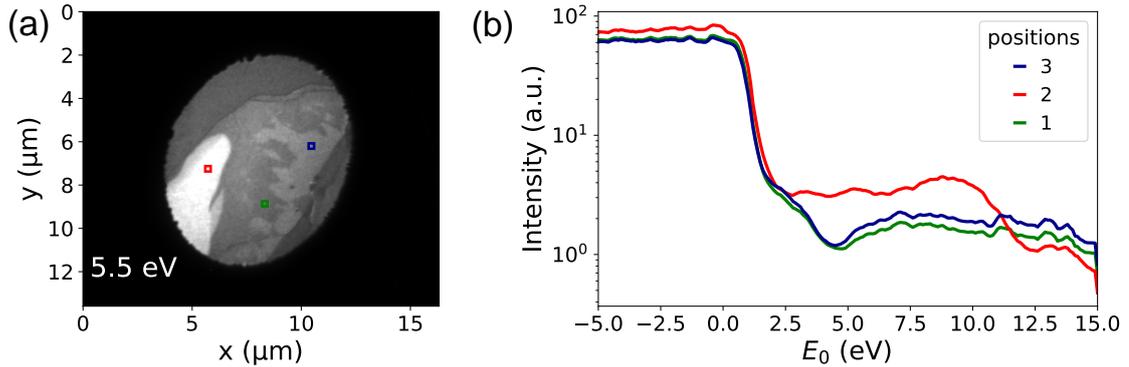

Figure B.3: (a): *Bright Field image of a NbSe₂ flake at 5.5 eV, where an intensity boundary between center and edge is visible.* **(b)**: *Real space IV curves at the marked spots on the flake in* **(a)**.

B.2   Roughness analysis with LEED

Section 3.5.1 gives a description of the method used to quantify the roughness. We measure line profiles for diffraction curve at the edge and center of the flake shown in figure 4.3a. Figure B.4 shows the line profile through the (0,0) LEED spot, measured perpendicular to dispersive direction.
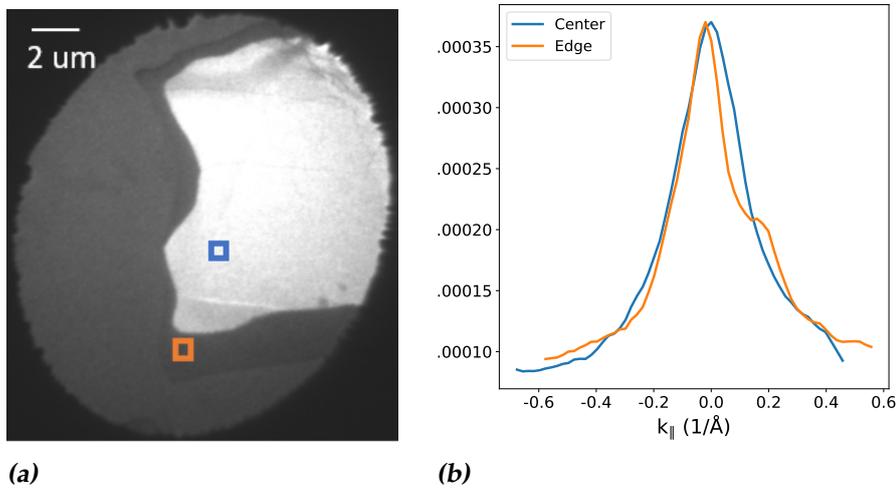
(a) *(b)*

Figure B.4: (a): *Bright Field LEEM image of a flake which shows an intensity boundary between center and edge.* **(b)**: *For the spots pointed out in figure B.4a, the intensity along a linecut through the (0,0) Low Energy Electron Diffraction spot is measured. Linecut taken perpendicular to the dispersive direction. Intensity is measured at 21.2 eV and plotted against $k_{\parallel}$.*

We see that the width of the peaks in figure B.4 is equal for the center and edge of the flake. Therefore, the plot demonstrates that the roughness is similar for both areas on the flake.

B.3   PCA results, after exposure to air.

We repeat the analysis described in section 3.5.2 for an IV dataset of the flake depicted in figure 4.3a. This IV measurement was performed after exposure to air (by venting in the load lock). The results are shown below. We clearly see that the field of view in figure B.5a measured with LEEM is different than in figures 4.10 and 4.11. This results in a different number of identified clusters: three instead of four. Namely, the flake at the bottom, visible in figure 4.5a, is not in the LEEM measurement window. Furthermore, the IV curves in figure B.5b exhibit the features from the center and edge (previously observed in figure 4.5b).
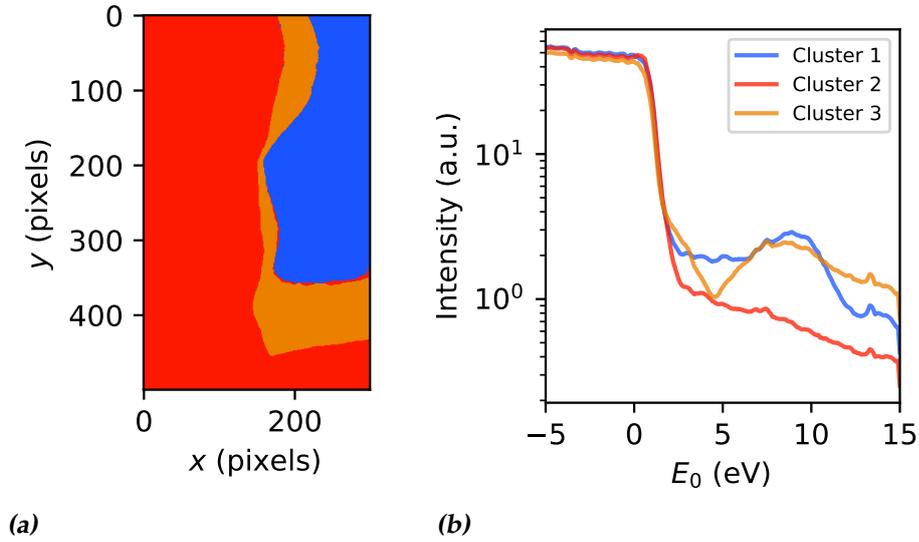
(a)   **(b)**

Figure B.5: *Result of PCA on flake in figure 4.5a, after exposure to air.* **(a):** *Reconstructed Bright Field image with three clusters.* **(b):** *IV curves of the clusters.*

B.4 Experiment motivated by contrast in optical microscope

The motivation for this experiment, is the remarkable colour contrast between and within flakes in figure 4.8. We hypothesized that this arose due to oxidation. *Ex situ* NbSe₂ samples on silicon with silicon dioxide were prepared and were exposed to air and light for 7 days. If the sample looked similar to the flakes in 4.8, the hypothesis was supported. After 7 days, the samples did not show the colours visible in figure 4.8, which is demonstrated in figure B.6 Therefore, we suspect the wide range of colours in figure 4.8 is due to the temperature in the LEEM: this sample was heated up to 600 °C, which could have caused to change optical properties.
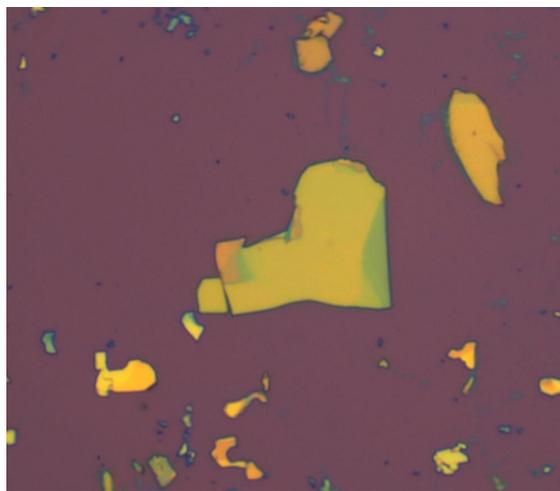
Figure B.6: *An optical microscope image of ex situ NbSe$_2$, after one week of exposure to air and light. While certain colours can be identified, the flakes do not resemble figure 4.8.*

Exposure of the *in situ* cleaved NbSe$_2$ to air

Additional experiments were performed to study the difference between exposure to pure oxygen and air. Figure C.1 shows that the IV curves did not alter upon venting the sample in the load lock. This supports the hypothesis that the
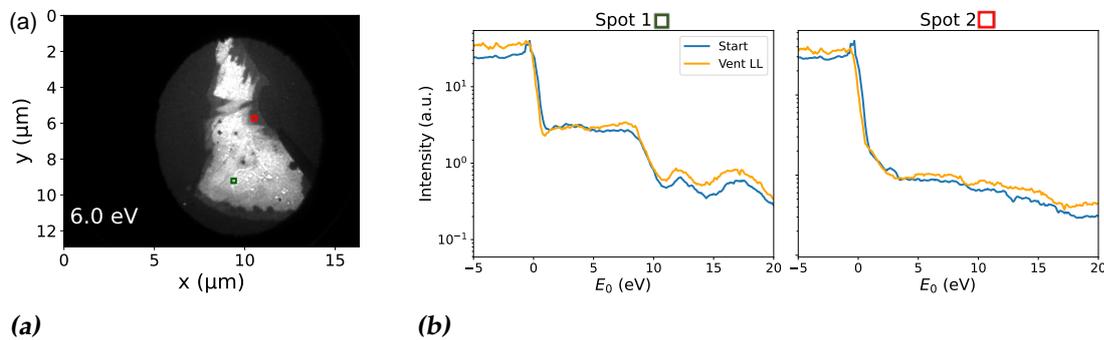

Figure C.1: (a): *Bright Field LEEM image a flake with an intensity boundary.* **(b)**: *Reflected intensity versus energy measured at the two locations in figure C.1a. We observe no development of the IV curves upon exposure to air (i.e., venting sample in the load lock)*

clean was flake before, and that the intensity boundary stems from contamination.

65

Appendix D

Method to obtain few-layer flakes of MoS$_2$

In this appendix, an alternative substrate is reviewed, which leads to thin TMD flakes.

We have tested this method to yield larger areas of thin flakes of MoS$_2$. To obtain few-layer TMDs, we use a different substrate. As a substrate, we start with silicon. Then, a 2 nm layer of gold is evaporated with niobium as sticking layer on top of our substrate. This method is described in [47]. The gold interacts with the chalcogen in the TMD layers (see figure 2.1), which results in thin flakes sticking to the gold.

We first used an optical microscope to analyze our result, an image is shown in figure D.1a. In figure D.1a, the large slightly darker areas suggest the presence of few-layer MoS$_2$ (see [47] for examples). To support, we have performed AFM on the samples. Because the contrast of the optical microscope in the AFM is not optimal, the thin areas are hard to distinguish. Consequently, a large thin flake area, like in figure D.1a, was not found. Figure D.1b shows a small thin flake, with a height of around 2 nm. From section 2.1, it is known that this corresponds to approximately three MoS$_2$ layers.

To conclude, the evaporation of gold on silicon substrate showed to yield thin flakes. During the research we did not take LEEM measurements on these samples, but this could be an object of future study.
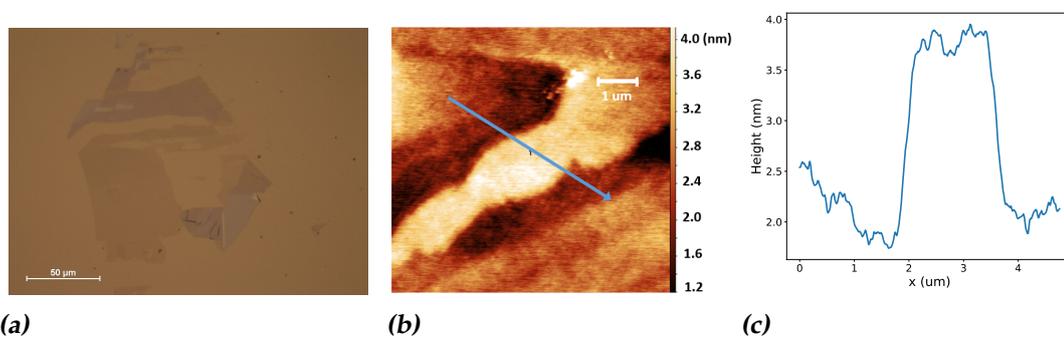
(a) **(b)** **(c)**

Figure D.1: (a): *Optical microscope image of MoS$_2$ flakes. On the silicon substrate, 2 nm of gold was evaporated with a sticking layer of niobium, to obtain thin MoS flakes.* **(b)**: *AFM image of a thin MoS$_2$ flake.* **(c)**: *Height profile along linecut. The height of the flake is approximately 2 nm*

.

Bibliography

[1] K. Klitzing, G. Dorda, and M. Pepper. New method for high-accuracy determination of the fine-structure constant based on quantized hall resistance. *Phys. Rev. Lett.*, 45(6):494–497, 08 1980. URL `https://doi.org/10.1103/PhysRevLett.45.494`.

[2] K.S. Novoselov, A.K. Geim, S.V. Morozov D. Jiang, Y. Zhang, S.V. Dubonos, I.V. Grigorieva, and A.A. Firsov. Electric field effect in atomically thin carbon films. *Science*, 306(5696):666–669, 2004. URL `https://doi.org/10.1126/science.1102896`.

[3] Y. Zhang, Y. Tan, H.L. Stormer, and P. Kim. Experimental observation of the quantum hall effect and berry's phase in graphene. *Nature*, 438(7065): 201–204, 11 2005. URL `https://doi.org/10.1038/nature04235`.

[4] K.S. Novoselov, A.K. Geim, S.V. Morozov, D. Jiang, M.I. Katsnelson, I.V. Grigorieva, S.V. Dubonos, and A.A. Firsov. Two-dimensional gas of massless dirac fermions in graphene. *Nature*, 438(7065):197–200, 11 2005. URL `https://doi.org/10.1038/nature04233`.

[5] K.I. Bolotin, K.J. Sikes, Z. Jiang, M. Klima, G. Fudenberg, J. Hone, P. Kim, and H.L. Stormer. Ultrahigh electron mobility in suspended graphene. *Solid State Communications*, 146(9):351–355, 2008. ISSN 0038-1098. URL `https://doi.org/10.1016/j.ssc.2008.02.024`.

[6] K.S. Novoselov, D. Jiang, F. Schedin, T.J. Booth, V.V. Khotkevich, S.V. Morozov, and A.K. Geim. Two-dimensional atomic crystals. *Proc Natl Acad Sci USA*, 102(30), 7 2005. URL `https://doi.org/10.1073/pnas.0502848102`.

[7] K.K. Kam and B.A. Parkinson. Detailed photocurrent spectroscopy of the semiconducting group vib transition metal dichalcogenides. *The Journal of*

Physical Chemistry, 86(4):463–467, 1982. URL `https://doi.org/10.1021/j100393a010`.

[8] K.F. Mak, C. Lee, J. Hone, J. Shan, and T.F. Heinz. Atomically thin mos₂: A new direct-gap semiconductor. *Phys. Rev. Lett.*, 105(13):136805, 9 2010. URL `https://doi.org/10.1103/PhysRevLett.105.136805`.

[9] B. Radisavljevic, A. Radenovic, J. Brivio, V. Giacometti, and A. Kis. Single-layer mos2 transistors. *Nature Nanotechnology*, 6:147–150, 3 2011. URL `https://doi.org/10.1038/nnano.2010.279`.

[10] O. Lopez-Sanchez, D. Lembke, D. Kayci, A. Radenovic, and A. Kis. Ultra-sensitive photodetectors based on monolayer mos2. *Nature Nanotech*, 8(7): 497–501, 2013. URL `https://doi.org/10.1038/nnano.2013.100`.

[11] Y. Liu, Y. Gao, S. Zhang, J. He, J. Yu, and Z. Liu. Valleytronics in transition metal dichalcogenides materials. *Nature Nanotechnology*, 6(11):147–150, 3 2011. URL `https://doi.org/10.1007/s12274-019-2497-2`.

[12] H. Qiu, L. Pan, Z. Yao, J. Li, Y. Shi, and X. Wang. Electrical characterization of back-gated bi-layer mos2 field-effect transistors and the effect of ambient on their performances. *Appl. Phys. Lett*, 100(12), 3 2021. URL `https://doi.org/10.1063/1.3696045`.

[13] Y. Zhang, Y. Kuwahara, K. Mori, C. Louis, and H. Yamashita. Hybrid phase 1t/2h-mos2 with controllable 1t concentration and its promoted hydrogen evolution reaction. *Nanoscale*, 12(22):11908–11915, 2023. URL `http://dx.doi.org/10.1039/D0NR02525A`.

[14] F.A. Lévy. *Crystallography and Crystal Chemistry of Materials with Layered Structures*. Physics and Chemistry of Materials with A. Springer Netherlands, 2012. ISBN 9789401014335. URL `https://books.google.nl/books?id=K0X8CAAAQBAJ`.

[15] H. Hibino, H. Kageshima, F. Maeda, M. Nagase, Y. Kobayashi, and H. Yamaguchi. Microscopic thickness determination of thin graphite films formed on SiC from quantized oscillation in reflectivity of low-energy electrons. *Phys. Rev. B*, 77(7):75413, 2 2008. URL `https://doi.org/10.1103/PhysRevB.77.075413`.

[16] S. Gokaran. Impossibility of the simple cubic metal in nature. 3 2018.

[17] P.S. Neu, M. Šiškins, E.E. Krasovskii, R.M. Tromp, and S.J. van der Molen. Electron transmission and mean free path in molybdenum disulfide at

electron-volt energies. *Phys. Rev. B*, 107(7):075427, 2 2023. URL `https://link.aps.org/doi/10.1103/PhysRevB.107.075427`.

[18] Transmission Electron Microscopy vs Scanning Electron Microscopy. Technical report, Thermofisher Scientific.

[19] V.A.E.C. Janssen. *Electronic properties of (pseudo-) two-dimensional materials*. Phd thesis, Leiden University, Huygens-Kamerlingh Onnes Laboratory, Leiden University P.O. Box 9500, 2300 RA Leiden, The Netherlands, 2020. URL `https://doi.org/10.4233/uuid:0c9f992c-7390-4d8f-aa6d-d89f0e7866a0`.

[20] J. Jobst, E.E. Krasovskii, R. Ribeiro, T.A. de Jong, C.R. Dean, R.M. Tromp, and S.J. van der Molen. Evolution of unoccupied bands in the series of MoX_2 transition metal dichalcogenides (x = s, se, te). unpublished, .

[21] J. Liu, J. Xiaofeng, C. Sun, and W. Zhu. Oxidation of the titanium(0001) surface: diffusion processes of oxygen from dft. *RSC Adv.*, 6(75):71311–71318, 2016. URL `http://dx.doi.org/10.1039/C6RA13877B`.

[22] Y.Kim, J. Huang, and C.M. Lieber. Characterization of nanometer scale wear and oxidation of transition metal dichalcogenide lubricants by atomic force microscopy. *Appl. Phys. Lett.*, 59(26):3404–3406, 1991. URL `https://doi.org/10.1063/1.105689`.

[23] H. Liu, N. Han, and J. Zhao. Atomistic insight into the oxidation of monolayer transition metal dichalcogenides: from structures to electronic properties. *RSC Adv.*, 5(23):17572–17581, 1 2015. URL `https://doi.org/10.1039/C4RA17320A`.

[24] G. Vacquier, A. Casalot, and A. Rolland. Superficial characterization of nbse2 single crystals: an auger electron spectroscopy study. *Materials Science and Engineering*, 85:L9–L12, 1987. ISSN 0025-5416. URL `https://doi.org/10.1016/0025-5416(87)90486-1`.

[25] J.E. Kim, V.T. Vu, T.T.H. Vu, T.L. Phan, Y.R. Kim, W.T. Kang, K. Kim, L.H. Lee, and W.J. Yu. A non-volatile memory based on nbox/nbse2 van der waals heterostructures. *Applied Sciences*, 10(21), 2020. ISSN 2076-3417. URL `https://doi.org/10.3390/app10217598`.

[26] L. Nguyen, H. Komsa, E. Khestanova, R.J. Kashtiban, J.J.P. Peters, S. Lawlor, A.M. Sanchez, J. Sloan, R.V. Gorbachev, I.V. Grigorieva, A.V. Krasheninnikov, and S.J. Haigh. Atomic defects and doping of monolayer

nbse2. *ACS Nano*, 11(3):2894–2904, 2017. URL `https://doi.org/10.1021/acsnano.6b08036`.

[27] M. Yamamoto, S. Dutta, S. Aikawa, S. Nakaharai, K. Wakabayashi, M.S. Fuhrer, K. Ueno, and K. Tsukagoshi. Self-limiting layer-by-layer oxidation of atomically thin wse2. *Nano Letters*, 15(3):2067–2073, 2015. URL `https://doi.org/10.1021/nl5049753`.

[28] J.C. Kotsakidis, Q. Zhang, A.L. Vazquez de Parga, M. Currie, K. Helmerson, D.K. Gaskill, and M.S. Fuhrer. Oxidation of monolayer ws2 in ambient is a photoinduced process. *Nano Lett.*, 19(8):5205–5215, 2018. URL `https://doi.org/10.1021/acs.nanolett.9b01599`.

[29] P. Budania, P. Baine, J. Montgomery, C McGeough, T. Cafolla, M. Modreanu, D. McNeill, N. Mitchell, G. Hughes, P. Hurley, and et al. Long-term stability of mechanically exfoliated mos2 flakes. *MRS Communications*, 7 (4):813–818, 2017. URL `https://doi.org/10.1557/mrc.2017.105`.

[30] G.E. Myers and G.L. Montet. Light-induced oxidation of nbse2 single crystals. *Journal of Physics and Chemistry of Solids*, 32(11):2645–2646, 1971. ISSN 0022-3697. URL `https://doi.org/10.1016/S0022-3697(71)80111-7`.

[31] J. Gao, B. Li, J. Tan, P. Chow, T. Lu, and N. Koratkar. Aging of transition metal dichalcogenide monolayers. *CS Nano*, 10(2):2628–2635, 2016. URL `https://doi.org/10.1021/acsnano.5b07677`.

[32] J.R. Lince and P.P. Frantz. Anisotropic oxidation of mos2 crystallites studied by angle-resolved x-ray photoelectron spectroscopy. *Tribology Letters*, 9 (3):211–218, 2001. URL `https://doi.org/10.1023/A:1018869107511`.

[33] R.M. Tromp, J.B. Hannon, W. Wan, A. Berghaus, and O. Schaff. A new aberration-corrected, energy-filtered leem/peem instrument ii. operation and results. *Ultramicroscopy*, 127:25–39, 4 2013. URL `https://doi.org/10.1016/j.ultramic.2012.07.016`.

[34] T.A. de Jong, D.N.L. Kok, A.J.H. van der Torren, H. Schopmans, R.M. Tromp, S.J. van der Molen, and J. Jobst. Quantitative analysis of spectroscopic low energy electron microscopy data: High-dynamic range imaging, drift correction and cluster analysis. *Ultramicroscopy*, 213:112913, 2020. ISSN 0304-3991. URL `https://doi.org/10.1016/j.ultramic.2019.112913`.

[35] S.R.A. el Tambouli. Low energy electron analysis and exfoliation techniques of transition metal dichalcogenides, 6 2023.

[36] SciPy. scipy.signal.wiener. URL `https://docs.scipy.org/doc/scipy/reference/generated/scipy.signal.wiener.html`.

[37] J. Goldstein. *Scanning Electron Microscopy and X-Ray Microanalysis*. Springer, 2003. ISBN 978-0-306-47292-3.

[38] M. Westerdijk. The growth and characterisation of a thin film caesium antimonide photocathode, 6 2023.

[39] Y. Gan. Atomic and subnanometer resolution in ambient conditions by atomic force microscopy. *Surface Science Reports*, 64(3):99–121, 2009. URL `https://doi.org/10.1016/j.surfrep.2008.12.001`.

[40] W. Jin and R.M. Osgood. Spectroscopic photoemission and low-energy electron microscopy studies of the surface and electronic structure of two-dimensional materials. *Advances in Physics: X.*, 4(1):1024–1056, 2019. URL `https://doi.org/10.1080/23746149.2019.1688187`.

[41] E.E. Krasovskii, W. Schattke, V.N. Strocov, and R. Claessen. Unoccupied band structure of nbse2 by very low-energy electron diffraction: Experiment and theory. *Phys. Rev. B.*, 66(23):235403, 7 2002. URL `https://doi.org/10.1103/PhysRevB.66.235403`.

[42] J. Konopka. Options for quantitative analysis of light elements by sem/eds. Technical report, Thermofisher Scientific. URL `https://assets.thermofisher.com/TFS-Assets/CAD/Warranties/TN52523_E_0713M_LightElement_H.pdf`.

[43] F. W. Smith and G. Ghidini. Reaction of oxygen with si(111) and (100): Critical conditions for the growth of sio2. *Journal of The Electrochemical Society*, 129(6):1300, 6 1982. URL `https://dx.doi.org/10.1149/1.2124122`.

[44] UK Anglo-Bell Company Limited. Niobium diselenide lubricant. *Vacuum*, 15(10):511, 1965. ISSN 0042-207X. URL `https://doi.org/10.1016/0042-207X(65)90361-1`.

[45] J.P. Landesman, A. Fiore, J. Nagle, V. Berger, E. Rosencher, and P. Puech. Local stress measurements in laterally oxidized gaas/alxga1âxas heterostructures by micro-raman spectroscopy. *Appl. Phys. Lett.*, 71(17):2520–2522, 10 1997. ISSN 0003-6951. URL `https://doi.org/10.1063/1.120420`.

[46] C.V. Raman and K.S. Krishnan. Polarisation of scattered light-quanta. *Nature*, 122(3066):169, 1928. URL `https://doi.org/10.1038/122169a0`.

[47] M. Heyl and E.J.W. List-kratochvil. Only gold can pull this off: mechanical exfoliations of transition metal dichalcogenides beyond scotch tape. *Appl. Phys. A*, 129(16), 2023. URL `https://doi.org/10.1007/s00339-022-06297-z`.

[48] H. Chen, Z. Li, X. Fan, L. Guo, and X. Chen. Quantum linear magnetoresistance in nbte2. *Solid State Communications*, 275:16–20, 2018. ISSN 0038-1098. URL `https://doi.org/10.1016/j.ssc.2018.02.019`.